Geometric and Thermodynamic Considerations of Saturated and Subcooled Liquid Nozzle Flow

Gregory G. Hendrickson[a*], Daniel K. Smith[b], Robert N. D'Alessandro[c], Georges A. Melhem[d], Marc E. Levin[e], Harold G. Fisher[f], Leonid Korelstein[g]

[a.*]Corresponding Author – Retired, 2018 Lazy Grove Drive, Kingwood, TX 77339, USA, email: greghendrickson1954@gmail.com
[b.]Albemarle Corporation, Gulf States Road, Baton Rouge, LA 70805, USA
[c.]Retired, Spanish Fort, AL 36527, USA
[d.]ioMosaic Corporation, 93 Stiles Road, Salem, NH 03079, USA
[e.]Independent Consultant, Spokane, WA, 99223, USA
[f.]Fisher Inc., 229 Brookhaven Drive, Nitro, WV 25143
[g.]Piping Systems Research & Engineering Company (NTP Truboprovod), Plehanova str., 7, Moscow, 111141, Russia

Keywords
Choked flow, non-equilibrium, bubble nucleation, superheating, rapid depressurization, metastability

Abstract
It is well known that homogeneous equilibrium methods for calculating the mass flux of initially subcooled or saturated liquids in short nozzles under-predict the measured values and various methods for estimating non-equilibrium effects have been presented in the past. It is shown in this paper that acceleration effects at the entrance of converging nozzles due to changing cross-sectional area can be the most significant cause of non-equilibrium. By properly accounting for non-equilibrium due to the fluid acceleration, single-phase flow methods can be used to estimate the pressure loss and mass flux in nozzles when rapid vaporization occurs at the nozzle throat. For these cases, choking occurs due to the rapid vaporization while the difference between the inlet pressure and choking pressure determines the nozzle mass flux.

1. Introduction

Thermal non-equilibrium phenomena have been recognized in the critical flow of fluids through short pipes and nozzles for several decades. According to Weisman and Tentner (1978), early studies of non-equilibrium include the works of Benjamin and Miller (1942), Burnell (1947), Hodkinson (1937) and Silver and Mitchell (1945). It is clear that there are at least two mechanisms of thermal non-equilibrium in subcooled/saturated/low-quality flow:

- Delay of vaporization (with metastable liquid) characteristic of subcooled/saturated inlet flow.
- Non-equilibrium vaporization (maybe after some delay of vaporization) for some relaxation period of time characteristic of low inlet quality flow.

The non-equilibrium phenomena addressed in this paper are the delay of vaporization and rapid phase transition associated with the rapid depressurization of initially slightly subcooled or saturated liquids.

2. Rapid Phase Transitions

When initially subcooled or saturated liquids are subjected to rapid pressure reduction below the liquid saturation pressure without bubble nucleation, the fluid is said to be superheated. The superheated state is thermodynamically metastable and typically the fluid begins to vaporize after a delay time which depends on the bubble nucleation rate. The bubble nucleation rate depends on the amount of superheating as described by bubble nucleation kinetic theory (Brennen, 1995). Correspondingly the amount of superheating is limited by thermodynamics. Thermodynamic stability analysis indicates phase change occurs spontaneously at the spinodal temperature (Lienhard *et al.*, 1986). Therefore, when a

fluid is highly superheated, the vaporization commences and proceeds at a rapid rate. The process of rapid phase transition is called explosive boiling. The same bubble nucleation kinetic and thermodynamic stability analyses apply to various phenomena including Rapid Phase Transitions (RPT), Boiling Liquid Expanding Vapor Explosions (BLEVE) and flow through nozzles. Examples of RPT applications are found in Melhem and Hendrickson (2020) while BLEVE applications are found in Mengmeng (2007). The focus of this paper is the application of bubble nucleation kinetics and thermodynamic stability analyses to the flow of subcooled and saturated liquids through nozzles. The proposed method addresses known deficiencies of the Homogeneous Equilibrium Model (HEM) by providing a method to quantify non-equilibrium effects on calculated nozzle choking pressures and critical mass flow rates.

3. Why Subcooled Flow Estimates Matter

Numerous plant design and hydraulic applications, including pressure relief systems, require reasonable flow rate estimates of initially saturated or slightly subcooled liquids. Current methods, such as the HEM, underestimate the flow rate depending on the degree of liquid subcooling. The consequence can result in underestimating leak rates for certain scenarios or the selection of significantly oversized relief devices for given overpressure scenarios. The problem is amplified when larger relief devices are installed and the downstream equipment for separation, flaring, and/or vent containment receive much higher flow rates than the design anticipated. Oversizing the relief devices can be costly and not knowing the flow rate accurately can be detrimental to the performance of downstream safety systems.

On the other hand, proper accounting of non-equilibrium flow phenomena offers a potential opportunity to save capital investments during pressure relief device revalidation projects. “Capacity creep” and debottlenecking projects in refineries and chemical plants can increase the required overpressure relief flow rate. It is not uncommon for the increased required flow rate to exceed the calculated capacity of installed pressure relief devices when equilibrium flow is assumed. It is foreseeable that accounting for the increased flow due to non-equilibrium effects can address seeming capacity deficiencies that would otherwise require modifications in the field (e.g., installing larger pressure relief devices).

4. Background

The fundamental equation for the determination of mass flux through a relief valve nozzle is the differential form of the steady-state, constant elevation and frictionless Bernoulli equation

$$udu = -vdP = -\frac{dP}{\rho} \tag{4.1}$$

Note: Variables are defined in the Nomenclature section. Integration from the stagnation state $(P = P_0, u = 0)$ to the nozzle throat (e.g., exit) pressure and expressing the result in terms of the mass flux yields

$$G = \rho_t \left[-2 \int_{P_0}^{P_t} \frac{dP}{\rho}\right]^{1/2} \tag{4.2}$$

Note this equation makes no provision for the geometry of the nozzle. This result becomes the Homogeneous Equilibrium Model (HEM) for nozzles when the flow is vapor-liquid two-phase flow and the following are assumed:

- The pressures in both phases are equal

- The temperatures in both phases are equal (thermal equilibrium)
- The velocities of both phases are equal (mechanical equilibrium)
- The Gibbs free energies (chemical potentials) of both phases are equal (chemical equilibrium)
- Homogeneity (the fluid is modeled as a single phase with thermodynamic properties that are the average of the two phases)

It has long been known that the HEM under-predicts the mass flux for nozzle flow with inlet conditions near the fluid saturation conditions. Early literature reviews presented by Saha (1978) and by Hsu (1972) indicate the HEM under-predicts critical discharge rates for short pipes and near saturation or subcooled upstream conditions due to the liquid superheat. An example from Hutcherson (1975) for flow with inlet qualities near zero is illustrated in Figure 4.1. The comparison shows that, as the inlet quality approaches zero, the error in the predicted critical mass flux increases.

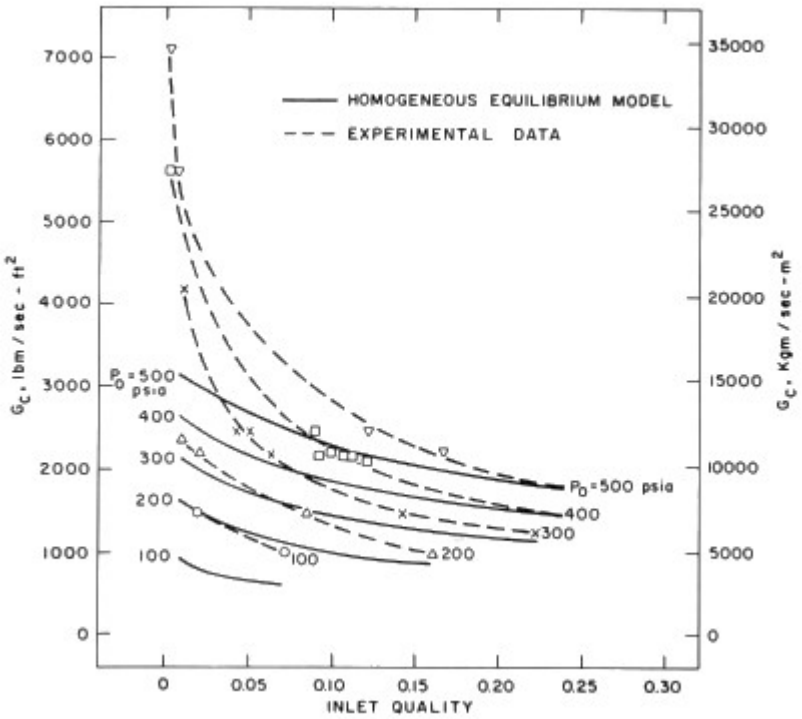

Figure 4.1, Comparison of HEM with Experimental Data from Hutcherson (1975, Figure 107)

When a subcooled or saturated liquid flow is analyzed using the HEM, pressure reduction along an isentropic flow path is nearly isothermal for small degrees of subcooling. However, the temperature increases slightly if the initial subcooling is achieved by increasing the pressure at constant entropy. Thus, as the initial pressure increases, depressurization along an isentropic flow path can result in some amount of temperature reduction with the amount of temperature reduction increasing as the initial pressure increases. In either case, the critical mass flux from application of Equation 4.2 with the equilibrium assumptions often occurs when the nozzle throat pressure is near the fluid saturation pressure. Isothermal depressurization from point A to point B located at the fluid saturation pressure is illustrated in Figure 4.2. The square at the top of the two-phase region represents the critical point.

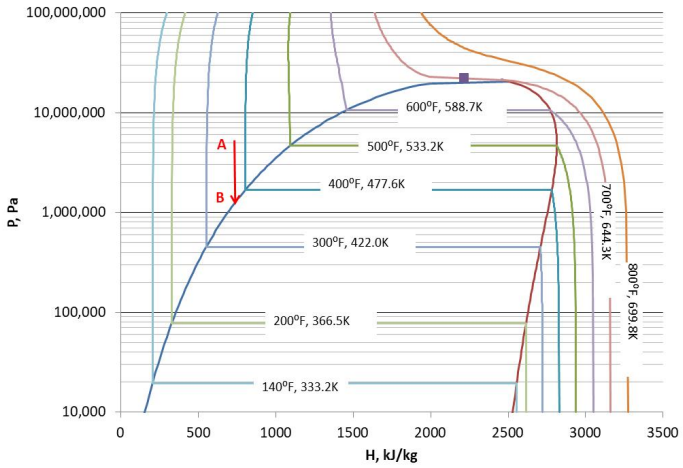

Figure 4.2, Flashing Commences near the Saturation Curve

When the fluid remains a saturated liquid for the majority of the flow path and the nozzle throat pressure is approximately equal to the fluid saturation pressure, a close estimate of the HEM flux can be obtained using the Bernoulli equation with the throat pressure equal to the saturation pressure.

$$G = \sqrt{2\rho_0(P_0 - P_s)} \tag{4.3}$$

See for example Leung and Ciolek (1994) who state that the use of the saturation pressure in the Bernoulli equation is appropriate due to choking at the throat for longer flow lengths (L/D=25, 50 and 100) when the HEM assumptions are appropriate. When frictional effects are included with constant elevation and thermodynamic equilibrium, the integrated Bernoulli equation becomes

$$G = \sqrt{\frac{2\rho_0(P_0 - P_s)}{1 + f_D\frac{l}{d}}} \tag{4.4}$$

In contrast, when non-equilibrium effects are important, the Bernoulli equation approximation to the HEM (Equations 4.3 or 4.4) under-predicts the critical mass flux for slightly subcooled and saturated liquid inlet conditions. The critical mass fluxes calculated using Equation 4.4 are compared with measured mass flux data for saturated and subcooled water flow from Sozzi and Sutherland (1975) in Figure 4.3. Inspection of Figure 4.3 reveals that the error in the calculated mass flux increases as the fluid subcooling decreases and as the nozzle length decreases. This deviation has been attributed to non-equilibrium effects. Note: inclusion of frictional effects is important for longer nozzles. The calculated mass flux is higher than the measured mass flux for longer nozzles and large subcooling when friction is ignored.

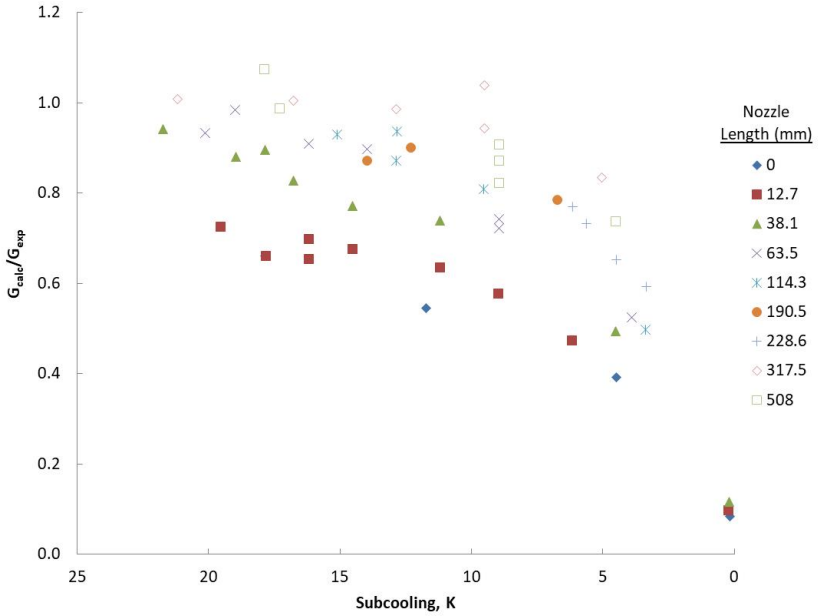

Figure 4.3, Comparison of Bernoulli Equation Calculated Flow with Sozzi and Sutherland (1975) Data

Various approaches have been proposed to more accurately predict the critical nozzle flow of saturated and subcooled liquids. Only four previous models are mentioned herein. For a more thorough summary, the reader is referred to Yoon *et al.* (2006).

4.1 Burnell Correction Factor

A method proposed by Burnell (1947) includes a correction factor, the Burnell C factor, in the Bernoulli equation.

$$G = \sqrt{2\rho_0[P_0 - (1-C)P_s]} \tag{4.1.1}$$

To account for friction, the $f_D l/d$ term can be retained.

$$G = \sqrt{\frac{2\rho_0[P_0-(1-C)P_s]}{1+f_D\frac{l}{d}}} \tag{4.1.2}$$

Examples from the literature for correlations of the Burnell C factor include Weisman and Tentner (1978), Sallet and Sommers (1985), and Kim (2015a). Weisman and Tentner (1978) show a correlation with the nozzle inlet saturation pressure for water flow (Figure 4.4). Sallet and Sommers (1985) reported a correlation with nozzle inlet stagnation temperature developed by Burnell (1947) for water flow.

$$C = 0.264\left[\frac{75.48-0.14T}{49.2}\right] \text{ where } T[=]°C \tag{4.1.3}$$

Sallet and Sommers (1985) also reported that Equation 4.1.3 was derived using a surface tension versus temperature correlation.

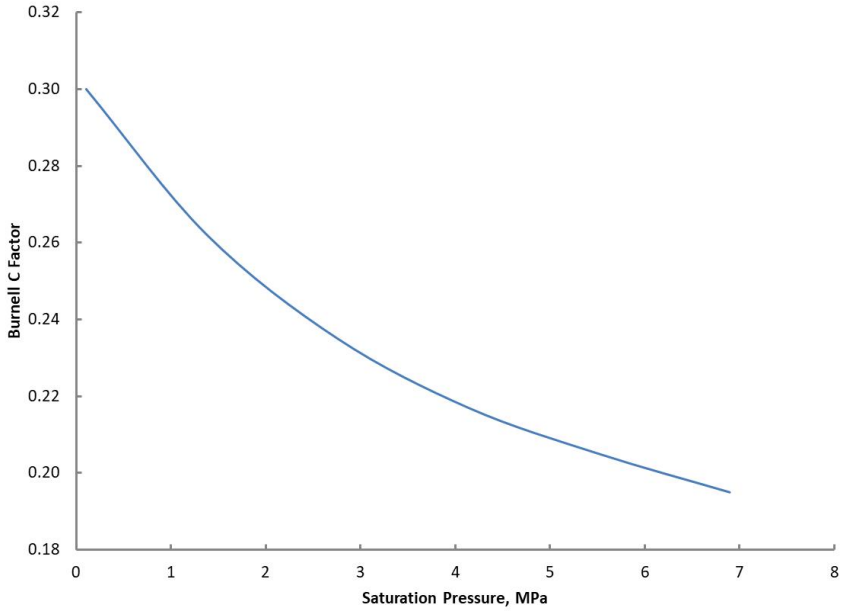

Figure 4.4, Weisman and Tentner (1978) Correlation for Burnell C Factor

4.2 Henry-Fauske Non-equilibrium Factor

As previously stated, deviation of the HEM from data for saturated and subcooled liquid flow has been attributed to non-equilibrium effects. Perhaps the first treatment of non-equilibrium effects in nozzle flow can be attributed to Henry and Fauske (1971). Henry and Fauske posited a "non-equilibrium" factor *N* such that the actual fluid quality (*x*) at the nozzle throat can be related to the equilibrium quality (x_E) at the nozzle throat.

$$\left(\frac{dx}{dP}\right)\Big|_t = N\left(\frac{dx_E}{dP}\right)\Big|_t \tag{4.2.1}$$

Equation 4.2.1 was developed using the no-slip condition at the nozzle throat and the presumption that $(dN/dP)\big|_t$ is negligible for constant area ducts and nozzles. The non-equilibrium factor was formulated as

$$N = \begin{cases} \frac{x_e}{0.14} \; for \; x_E < 0.14 \\ 1 \; for \; x_E \geq 0.14 \end{cases} \tag{4.2.2}$$

Sudi *et al.* (1994) pointed out that Jones & Saha (1977) and Jones (1980, 1982) showed Henry & Fauske's model could not explain the relaxation process in which superheated liquid proceeds toward a saturated state via vaporization. They suggest that Equation 4.2.1 is contrary to results obtained from basic mass conservation and that the real relaxation phenomena are governed by interfacial processes independent of the equilibrium path driving the phase change.

4.3 Leung Extension of Henry-Fauske Method

Leung (2019) extended the method of Henry and Fauske using his ω-method to calculate the equilibrium quality and then adjusting the equilibrium quality with a Henry-Fauske type non-equilibrium factor.

Leung developed correlations for the non-equilibrium factor for several data sets. His observations include:

- Thermal equilibrium is closely approached for inlet quality greater than 0.1 ($x_o > 0.1$)
- Thermal non-equilibrium does not play a significant role at high inlet sub-cooling (Bernoulli flow)
- The largest thermal non-equilibrium occurs at the saturated inlet condition ($x_o = 0$) due to the bubble nucleation process
- Pressure-undershoot occurs, i.e. pressure dropping below the saturation pressure, at flashing inception

Leung's contribution was application of the ω-method to estimate the Henry-Fauske non-equilibrium factor.

4.4 Delayed Equilibrium Model

Another approach to modeling non-equilibrium flow is the Delayed Equilibrium Model (DEM) as described by Bartosiewicz *et al.* (2011) and De Lorenzo *et al.* (2017). The presence of three phases is assumed in the DEM: saturated vapor, saturated liquid and a metastable liquid. In the DEM, the fluid pressure decreases to the saturation pressure (P_s) due to acceleration and friction but flashing does not commence until a lower onset pressure (P_o). Between the saturation pressure and the flashing onset pressure, the fluid is referred to as metastable fluid. Bartosiewicz *et al.* (2011) report observations by Lackmé (1979) that the onset pressure is 0.95 – 0.98 times the saturation pressure and used a factor of 0.95. Reducing the flashing onset pressure has the effect of shifting the onset of nucleation to a pressure less than the saturation pressure. The metastable fluid phase does not disappear instantaneously after the flashing onset pressure is reached, but rather is converted to an equilibrium phase based on an empirical relaxation law. The resulting fluid quality depends on the rate of relaxation of the metastable fluid to the equilibrium fluid. Bartosiewicz *et al.* (2011) report their approach is similar to the Homogeneous Relaxation Model (HRM) of Bilicki (1990).

4.5 Summary

To summarize, the flow of saturated and slightly subcooled liquids in nozzles is characterized by a rapid pressure decrease to a non-equilibrium superheated state. The superheated liquid is referred to as a metastable fluid. Upon depressurization, flashing does not typically commence until the fluid pressure falls below the fluid saturation pressure. The amount of pressure-undershoot (or equivalently, the amount of fluid superheating) is determined by non-equilibrium phenomena. The commonality of the various methods (Burnell, Henry and Fauske, Leung, DEM) is that upon depressurization a metastable fluid is produced. The Burnell method can be thought of as representing single-phase metastable fluid flow into the two-phase envelope until rapid vaporization occurs at the nozzle throat. The Henry–Fauske and Leung methods can be viewed as reducing the quality for a given throat pressure. The empirical non-equilibrium factor (N) is determined such that the mass flux is calculated with acceptable accuracy. The DEM combines both boiling delay (until the flashing onset pressure) and a reduced quality at the nozzle throat based on a relaxation model. The thermodynamic path of depressurization into the two-phase region is illustrated in Figure 4.5. As the pressure is reduced from Point A to Point B a metastable fluid is formed when the fluid pressure decreases below the saturation pressure. Vaporization commences and choking occurs at Point B rather than at the saturation pressure. The square at the top of the two-phase envelope represents the critical point.

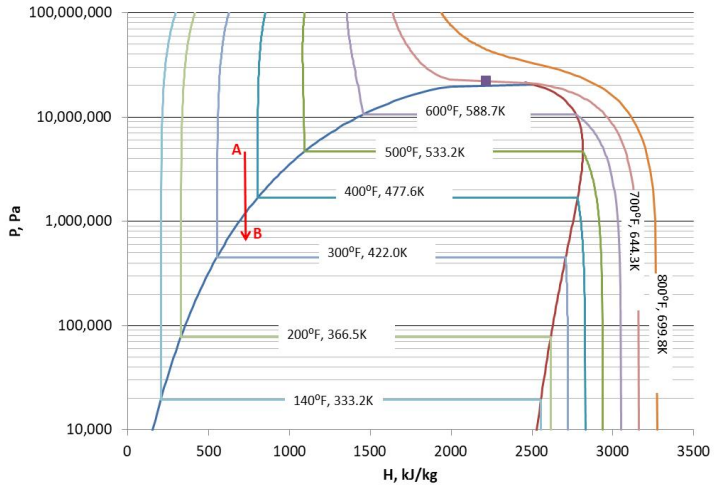

Figure 4.5, Flashing Commences inside the Two-Phase Envelope

5. Non-equilibrium Flow Model Description

A premise of the proposed calculation method is that when saturated and slightly subcooled liquids flow through converging nozzles, the observed non-equilibrium effects are a manifestation of the rapid depressurization upon acceleration of the fluid in the nozzle converging section. It has been demonstrated in bubble nucleation literature, see for example Alamgir and Lienhard (1981), that the amount of pressure-undershoot (e.g., superheating) depends on the rate of depressurization. The difference between the fluid saturation pressure and the bubble nucleation pressure increases as the depressurization rate increases. In nozzle flow the rate of depressurization is related to the rate of fluid acceleration and thus also to the geometry of the converging flow area. In other words, the amount of thermal non-equilibrium is determined by the nozzle geometry and rate of acceleration pressure decrease. When rapid vaporization occurs at the nozzle throat, the nozzle throat pressure can be represented by the bubble nucleation pressure. Further, it will be shown that Burnell's C factor can be correlated with the rate of depressurization due to acceleration into the nozzle.

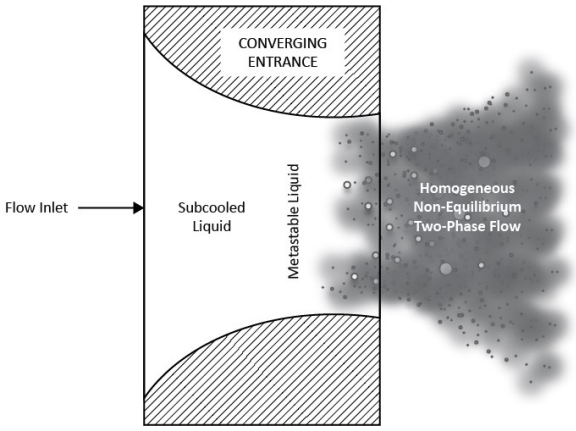

Figure 5.1, Generic Converging Nozzle

The proposition is illustrated using a generic converging nozzle (Figure 5.1) and described as follows. *Note the same principles also apply to square-edged inlets if the vena contracta is properly accounted for as discussed in the Prisco data analysis below.* The fluid is accelerated in the converging section of the nozzle due to the pressure driving force. The rate of this acceleration pressure loss determines the amount of superheating, e.g., the undershoot pressure, as determined by the bubble nucleation pressure. For a given overall pressure drop, as the friction loss in the straight section of the nozzle increases, the amount of pressure drop available for acceleration loss in the converging section decreases, i.e., increasing the length of the straight section of the nozzle downstream of the converging section decreases the acceleration losses in the converging section. *Thus, the departure from equilibrium in the converging section decreases as the friction loss in the straight section increases.* This interpretation is consistent with the rule of thumb that equilibrium flow occurs when the nozzle length is greater than 100 mm (4 inches); namely, the length provides enough friction loss (e.g., back pressure) to cause the bubble nucleation pressure to approach the fluid vapor pressure in the converging section. Furthermore, for a range of nozzle lengths, the friction losses of the metastable fluid in the straight section of the nozzle can be represented by the single-phase Darcy–Weisbach equation (Equation 5.1) and choking occurs due to rapid vaporization essentially at the nozzle throat. The Darcy-Weisbach equation can be used to compute pressure drop for laminar or turbulent flow using an empirical friction factor (Benedict, 1980).

$$\Delta P = f_D \frac{l}{d} \frac{\rho u^2}{2 g_c} \tag{5.1}$$

This interpretation is consistent with observations that flashing primarily occurs near the location of minimum pressure (Shin and Jones, 1993), e.g., the nozzle throat.

The characteristics of fluid flow in a nozzle as depicted by Fauske (1962) are illustrated in Figure 5.2. In Figure 5.2, the nozzle length is represented by the vertical line. Pressure "upstream" of the nozzle exit is represented by the curves to the left of the vertical line. Pressure downstream of the nozzle exit is to the right of the vertical line. In this view of nozzle flow, the pressure drop is linear with axial distance for a large portion of the nozzle. Line III corresponds to a typical pressure profile in which critical flow conditions do not exist. For the flow of saturated and subcooled liquids through a nozzle, this pressure profile can be represented by the Bernoulli equation for single-phase flow. Line I represents critical flow with a finite critical pressure profile. Fauske (1962) cites data indicating the slope of the pressure profile for constant mass flux and quality, i.e., $(dP/dz)|_{G,x}$, is finite.

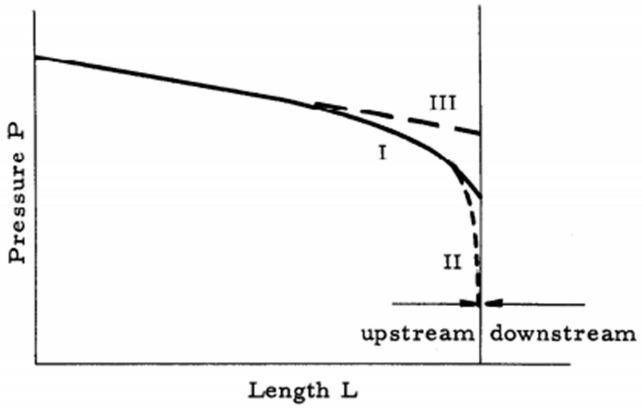

Figure 5.2, Characteristics of Critical Flow (from Fauske, 1962, Figure 18)

Line II represents the mathematical treatment of critical flow in which *dP/dz* at the throat is infinite. In this mathematical representation of saturated or subcooled flow, the pressure profile is linear for essentially the entire nozzle length. Choking is indicated when then the calculated slope rapidly approaches negative infinity a short distance from the outlet. This pressure profile would be typical of the HEM, for example. In this view of critical flow, "rapid vaporization" occurring at the nozzle throat is responsible for choking the flow.

The Bernoulli equation with the throat pressure equal to the vapor pressure (Equation 4.4) can be used to estimate the mass flux when single-phase flow occurs over most of the nozzle length and equilibrium flashing approximately coincident with choking occurs essentially only at the nozzle throat. This view of choking is commonly accepted for equilibrium flow of subcooled and saturated fluids. It will subsequently be shown that, by application of bubble nucleation dynamics to estimate the nozzle throat pressure, the Bernoulli equation with the throat pressure equal to the bubble nucleation pressure can be used to estimate the mass flux when single-phase flow occurs over most of the nozzle length and non-equilibrium flashing approximately coincident with choking occurs essentially only at the nozzle throat. *The difference between the flow of equilibrium fluids and metastable fluids in nozzles is that equilibrium fluids flash at the thermodynamic vapor pressure while metastable fluids flash at a pressure lower than the thermodynamic vapor pressure.* Of course, the first step is formation of the metastable fluid.

6. Overview of Bubble Nucleation and Growth

Vapor bubbles can only form if sufficient energy is available to overcome the cohesive forces of the liquid and create a void space for the vapor. Bubbles with sufficient energy to attain a critical size can survive and grow to larger sizes while bubbles with insufficient size collapse. Nucleation is the formation of the critically sized or larger bubbles. The radius of a spherical bubble of this sufficient size is known as the critical radius.

Figure 6.1 illustrates the three phases of bubble growth in superheated liquids. Bubble nucleation commences after a finite delay time. Upon nucleation, the bubble radius is just larger than the critical radius. Initially surface tension impedes bubble growth. After the bubble grows somewhat (Miyatake *et al*. (1997) suggest doubling the diameter), inertia forces dominate and the bubble growth is primarily due to the difference in the pressure of the vapor inside the bubble and the fluid pressure exterior to the bubble. The pressure of the vapor inside the bubble is related to the local fluid thermodynamic vapor pressure by the Poynting correction factor. During this phase the bubble growth is approximately linear with respect to time. As the bubble grows further, its temperature drops causing a temperature difference between the surrounding fluid and bubble interior. In this phase the bubble growth rate is dominated by heat transfer from the surrounding liquid, which causes the addition of vapor to the bubble by evaporation at the vapor-liquid interface. During this phase the bubble growth is approximately proportional to the square root of time.

Common assumptions in equilibrium models of two-phase flow cannot account for bubble dynamics when the bubble nucleation delay time is significant compared to the fluid residence time in the nozzle and when significant pressure and temperature differences exist between the liquid and vapor phases. According to Yoon *et al.* (2006), thermal non-equilibrium has been shown to be related to bubble nucleation because several researchers used a nucleation delay time on the order of 1 ms in homogeneous non-equilibrium models to predict experimental results. Bubble nucleation delay is

consistent with experimental results and provides an explanation for rapid phase transition phenomena. The challenge is to relate bubble nucleation phenomena to nozzle flow phenomena.

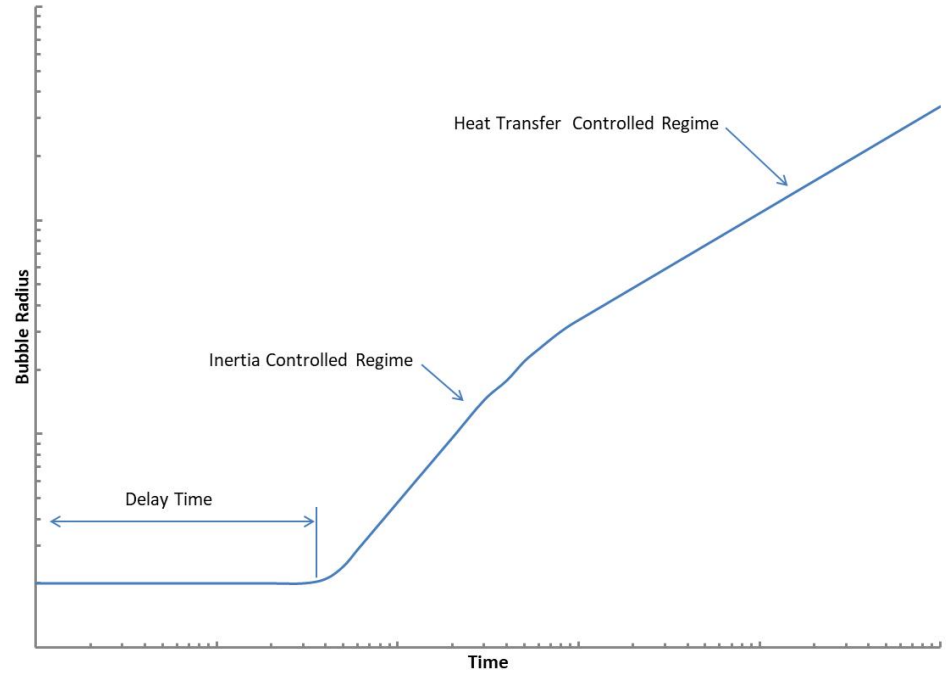

Figure 6.1, Bubble Growth Development

7. Metastable Fluid Formation and Bubble Nucleation in Nozzle Flow

The importance of non-equilibrium effects in nozzle flow has long been recognized. According to Angelo *et al*. (2012), the idea of a metastable fluid is not new; rather it was introduced by Silver and Mitchell (1951). Because the degree of superheat is directly related to the amount of pressure decrease below the saturation pressure, these concepts can be used interchangeably to describe deviation from equilibrium upon pressure reduction.

In classical homogeneous bubble nucleation theory (Brennen,1995), the net work required to form a bubble having the critical size is

$$W_{cr} = \frac{16\pi\sigma^3}{3(\Delta P)^2} \tag{7.1}$$

In this expression ΔP is the difference between the equilibrium pressure inside the bubble and the pressure of the liquid surrounding the bubble.

The relationship between the net work to form a bubble and the typical kinetic energy of the molecules, e.g., *kT*, is typically given in terms of the Gibbs number

$$Gb = W_{cr}/kT \tag{7.2}$$

Combining Equations 7.1 and 7.2 to eliminate the work term results in

$$Gb = \frac{16\pi\sigma^3}{3kT(\Delta P)^2} \tag{7.3}$$

In addition to homogeneous nucleation in the bulk liquid, heterogeneous nucleation also occurs on the surfaces of the flow channel and on minute particles or bubbles. It is recognized that heterogeneous nucleation occurs in nozzle flow and, at least in the beginning, is the dominant source of bubble formation (Riznic *et al.*, 1987). A bubble nucleation heterogeneity factor, φ, is typically included in Equation 7.3 to account for heterogeneous nucleation.

$$\frac{Gb}{\varphi} = \frac{16\pi\sigma^3}{3kT(\Delta P)^2} \tag{7.4}$$

The challenge in applying Equation 7.4 to nozzle flow is determination of the heterogeneity factor.

The pressure difference in Equation 7.1 can be related to the vapor pressure of the fluid at the liquid temperature using the Poynting correction factor. Application of the Poynting correction factor is given by the following approximate expression (Blander and Katz, 1975).

$$\Delta P = [P_s(T_i) - P_n]\left(1 - \frac{v_f}{v_g}\right) \tag{7.5}$$

Credit has been given to Alamgir and Lienhard (1981) for first examining pressure-undershoot. They developed a semi-empirical correlation, motivated by classical nucleation theory, to predict the pressure-undershoot below the saturation pressure at the onset of flashing during the rapid depressurization of hot water. Alamgir and Lienhard used *Gb*=28.2 and developed the depressurization rate, Σ', dependent heterogeneity factor correlation given by Equation 7.6. The resulting pressure-undershoot correlation is given by Equation 7.7.

$$\varphi = 0.1058T_r^{28.46}[1 + 14(\Sigma')^{0.8}] \tag{7.6}$$

Equation 7.7 is derived by substitution of Equations 7.6 and 7.5 into Equation 7.4 and setting *Gb*=28.2. For convenience, this equation will be referred to as the "Alamgir and Lienhard (A-L) correlation".

$$P_s(T_i) - P_n = 0.252\frac{\sigma^{3/2}T_r^{13.73}\left[1+14(\Sigma')^{0.8}\right]^{1/2}}{\sqrt{kT_c}\left(1-\frac{v_f}{v_g}\right)} \tag{7.7}$$

Note: Lienhard *et al.* (1986) provided a review of equations of state and the prediction of spinodal lines and incorrectly showed the quantity (1-v_f/v_g) under the square root sign (their Equation 28). The term should be outside the square root sign as shown in Equation 7.7. This correction is consistent with the original Alamgir and Lienhard (1981) correlation (their Equation 13) and with Equations 7.8 and 7.12. Also note the precise value of the constant in front of Equation 7.7 is 0.2507 rather than 0.252. When reference is made to the Alamgir and Lienhard correlation their value of 0.252 is retained.

The Alamgir and Lienhard correlation is dimensional, with depressurization rate units of Matm/s (Mega-atm/s). Surface tension, Boltzmann constant, temperature and pressure units are self-consistent. The correlation was developed for

$$0.62 \le T_r \le 0.935 \; and \; 0.004 \le \Sigma' \le 1.8 \; Matm/s \; (405 \; \le \Sigma' \le 182{,}000 \; MPa/s)$$

The model cannot be used to accurately predict the nucleation pressure for smaller depressurization rates without changing the correlation constants. The heterogeneity factor given in Equation 7.6 was developed for water. It will be demonstrated later that it can also be used for other chemicals, including mixtures, with proper scaling of the Gibbs number.

Abuaf *et al.* (1983) stated that "according to accepted concepts" for nozzle flow with subcooled inlet conditions, the liquid accelerates in the converging section causing the local pressure to drop below the saturation pressure. The resulting metastable superheated fluid flow is essentially a single phase until it reaches the flashing inception point. Abuaf *et al.* utilized the correlation developed by Alamgir and Lienhard combined with a correlation for turbulence intensity to demonstrate the flashing inception point is essentially located at the plane of minimum cross-sectional area in converging-diverging nozzles.

Abuaf *et al.* defined a static flashing pressure-undershoot and a dynamic pressure-undershoot. They estimated the static flashing pressure-undershoot value using a slightly modified version of the Alamgir and Lienhard correlation, Equation 7.8. (Note: The nomenclature of Abuaf *et al.* is retained in Equation 7.8. The static flashing pressure in Equation 7.8 is equivalent to the nucleation pressure in Equation 7.7.)

$$\Delta P_{Fio} = P_s - P_{Fi} = 0.253 \frac{\sigma^{3/2}}{\sqrt{kT_c}} \frac{T_r^{13.73} \sqrt{1+1\ (\Sigma')^{0.8}}}{\left(1-\frac{v_f}{v_g}\right)} \tag{7.8}$$

A dimensionless pressure-undershoot at flashing inception was defined to relate the static flashing pressure-undershoot (ΔP_{Fio}) to the dynamic pressure-undershoot (ΔP_{Fi})

$$\Delta P_{Fi}^* = \frac{\Delta P_{Fi}}{\Delta P_{Fio}} \tag{7.9}$$

The dimensionless pressure-undershoot was defined as a function of the turbulence intensity and for converging flows as a function of the area ratio. The turbulence effects were then shown to be small for the converging flow data set examined and were subsequently neglected, namely $\Delta P_{Fi}^* \sim 1$ with the static pressure-undershoot approximately equal to the dynamic pressure-undershoot. With flashing inception at the nozzle throat, single-phase flow can be considered upstream of the throat. For liquids with constant density, the critical mass flux was then given by

$$G_c = C_D \sqrt{2\rho(P_0 - P_s + \Delta P_{Fi})} \tag{7.10}$$

The depressurization rate for nozzles was given as

$$\Sigma' = \frac{G_c^3}{\rho^2} \frac{d(lnA)}{dz} + \Sigma'_0 \tag{7.11}$$

In this expression for the depressurization rate, frictional loss has been neglected and Σ'_0 is a transient component equal to zero for steady flows. Where discharge pressure measurements were available, a discharge coefficient (C_D) of 0.94 was found to fit the data within 4%. For the data of Powell (1961), the throat pressure was not given, but Abuaf *et al.* were able to fit the flow data within 5% by using a discharge coefficient of 0.90.

Levy & Abdollahian (1982) used a slight modification to the Alamgir and Lienhard correlation based on the data of Reocreux (1974). Their final expression for the critical flow rate was virtually identical to those proposed by both Alamgir and Lienhard (1981) and Abuaf *et al.* (1983).

$$\Delta P_d = 0.258 \frac{\sigma^{3/2}}{\sqrt{kT_c}} \frac{T_r^{13.76}\sqrt{0.49+13.25(\Sigma')^{0.8}}}{\left(1-\frac{v_f}{v_g}\right)} \tag{7.12}$$

In the Levy and Abdollahian model, the flashing inception occurs when the liquid pressure reaches an amount ΔP_d below the saturation pressure corresponding to the liquid temperature. Levy and Abdollahian used an average decompression rate over the length of the nozzle.

$$\bar{\Sigma} = \frac{1}{4}(G_t + G_e)\left[\left(\frac{G}{\rho}\right)_t^2 - \left(\frac{G}{\rho}\right)_e^2\right]/\Delta z \tag{7.13}$$

The subscripts "t" and "e" correspond to throat and entrance, respectively, and Δz is the nozzle length. A critical assumption by Levy and Abdollahian (1982) is that a constant amount of superheat is maintained as the pressure decreases along the flow path through the nozzle, i.e., it did not account for any relaxation phenomena. They claimed the assumption of maintaining the liquid in non-equilibrium conditions is supported by the substantial relaxation times that could be inferred from the Marviken full-scale critical flow test data (Marviken, 1982). They also concluded their model results agree with the data when the nozzle contraction zone is followed by a short constant-area section.

The methods described for water by Alamgir and Lienhard (1981), Abuaf *et al.* (1983) and Levy and Abdollahian (1982) form the basis for the method described in this paper. The proposed method uses the Alamgir and Lienhard (1981) heterogeneity factor (Equation 7.6) to estimate the nozzle throat pressure. Contributions to the art include application of the depressurization rate equation (Equation 7.11) to both a converging nozzle and a sudden contraction at the point in the nozzle where the maximum depressurization rate occurs. The method applies to a sudden contraction by accounting for the depressurization rate in the *vena contracta*. Thus the method provides a relationship between nozzle geometry and the amount of pressure-undershoot. Finally, it is recognized that the nucleation pressure estimated using Equation 7.7 represents the minimum nozzle throat pressure when rapid vaporization occurs at the nozzle throat. Sufficient pressure driving force must be available for the depressurization due to acceleration to achieve the minimum nozzle throat pressure. If sufficient pressure driving force is not available, then the potential pressure-undershoot given by Equation 7.7 is not fully realized and an "approach to equilibrium" factor is utilized. The method is called herein the "bubble nucleation method".

8. Relaxation Time

The conceptual model proposed for initially subcooled and saturated liquid flow through a converging nozzle is described by single-phase flow over the length of the nozzle with flashing, and choking, occurring at the nozzle throat. Application of the proposed model should be limited to situations where superheated fluid (*i.e.*, metastable fluid) flow occurs over essentially the entire length of the nozzle and flashing occurs at the nozzle throat. Shin and Jones (1993) pointed out that treating the flashing inception as a single point has been previously justified since in many cases, such as converging-diverging nozzles, flashing occurs in a zone that is quite narrow. However, in other cases, such as constant-area flows with friction-dominated pressure profiles, the flashing may continue over a wider range of the nozzle length. This effect makes it important to determine both the size and number of

bubbles locally so that accurate estimation of the development of void fraction may be undertaken. In this regard, it is important to determine the relaxation time phenomena.

Moody (1975) and Fauske (1985) indicated for subcooled and saturated inlet conditions, flashing water-steam flow approaches equilibrium conditions for flow lengths larger than about 100 mm (4 inches). Kim (2015b) indicated the criterion could be 127 mm (5 inches) for sub-cooled and two-phase water, but should be changed to 305 mm (12 inches) for saturated water. Kim (2015b) also suggested an L/D ratio of 25 as a criterion for the transition from non-equilibrium choking to equilibrium choking for nozzle and pipe flashing water-steam flows. In contrast, Nilpueng and Wongwises (2009) studied the flow of HFC-134a through short tube orifices and observed metastable liquid flow at the tube central core surrounded by two-phase bubble flow followed by two-phase bubble flow after the metastable core disappeared. The length of the metastable core increased with the amount of subcooling but had disappeared before the end of the 15 mm (0.6 inch) long tubes used in their studies.

Downar-Zapolski *et al.* (1996) defined the relaxation time, Θ, in terms of quality for use in the Homogeneous Relaxation Model (HRM).

$$\frac{Dx}{Dt} = \frac{\partial x}{\partial t} + u\frac{\partial x}{\partial z} = -\frac{x-\bar{x}}{\theta} \tag{8.1}$$

Locally, in a Lagrangian description of the flow, the relaxation equation exhibits an exponential approach to equilibrium from an initial state x_0.

$$x = x_E - (x_E - x_0)exp\left(\frac{-t}{\theta}\right) \tag{8.2}$$

Correlation of the "Moby Dick" data (Reocreux, 1974) resulted in a correlation for pressures up to 10 bar(a) of the form

$$\theta = 6.5x10^{-4}\epsilon^{-0.257}\psi^{-2.24} \tag{8.3}$$

For pressures above 10 bar(a) the correlation took the form

$$\theta = 3.84x10^{-7}\epsilon^{-0.54}\varphi^{-1.76} \tag{8.4}$$

In these correlations the non-dimensional pressure differences are defined as

$$\psi = \frac{P_s(T_{in})-P}{P_s(T_{in})} \tag{8.5}$$

$$\varphi = \frac{P_s(T_{in})-P}{P_c-P_s(T_{in})} \tag{8.6}$$

Downer-Zapolski *et al.* (1996) indicated that for θ=1 second, the predictions of the HRM are equivalent to the Homogeneous Frozen Model (HFM) and for θ=0.001 second (1 ms), the HRM predictions are equivalent to the Homogeneous Equilibrium Model (HEM). *An implication for subcooled and saturated liquid flow in nozzles is that relaxation time, not length or length/diameter ratio, should be the criterion for approach to equilibrium.*

Sudi *et al*. (1994) studied the relaxation time of water in a 4.95 mm (0.19 inch) inside diameter by 1,055 mm (41.5 inches) long stainless steel tube. They defined the relaxation time as the time between the saturation inception point and the relaxation inception point. Effectively the saturation inception point is when the fluid reaches its bubble point pressure at the inlet temperature. The relaxation inception point was determined in their experiments by noting when the liquid temperature starts to decrease along with the liquid pressure. *Their data showed required relaxation lengths between 350 and 450 mm (14 and 18 inches) and corresponding relaxation times between about 55 and 85 ms.*

For short nozzles or long relaxation times, it is expected that the flow over the majority of the nozzle length can be considered "frozen flow", where no vaporization occurs. However, for subcooled or saturated liquid flows that have experienced rapid pressure loss, the "frozen flow" regime is characterized by the formation of a metastable fluid phase. Unfortunately, the physical properties of metastable fluids are not generally known and thus the saturated liquid properties are used in the Downer-Zapolski *et al.* (1996) correlation.

9. Explosive Vaporization

For single-phase flow, it is accepted that a pressure discontinuity occurs at the nozzle throat when the flow is choked. For short nozzles with subcooled or saturated liquid feed, a similar rapid depressurization and pressure discontinuity has been observed near the nozzle throat. The extreme pressure gradient at the nozzle outlet, see for example line II in Figure 5.2, is characterized by rapid vaporization at the nozzle outlet when the metastable fluid pressure decreases to below the flashing inception pressure. For these cases, flashing inception occurs essentially at the nozzle throat. Simões-Moriera and Shepard (1999), Vieira and Simões-Moriera (2007), and Angelo *et al*. (2012) suggest the sonic flow state can be determined using the Chapman-Jouget (C-J) condition with a Rankine–Hugoniot jump condition. Application of the C-J condition is outside the scope of this paper but the concept of rapid vaporization coincident with choking at the nozzle throat is incorporated in the model assumptions.

10. Thermodynamic Considerations

The amount of superheating upon rapid depressurization of a subcooled or saturated liquid is constrained by the fluid thermodynamic properties. A depressurization diagram is illustrated in Figure 10.1 for water. The upper (or leftmost) curve represents the water saturation pressure and the lower (or rightmost) curve represents the liquid thermodynamic stability limit, called the spinodal curve. The curves in between represent the expected pressure-undershoot below the saturation pressure using the Alamgir and Lienhard correlation (Equation 7.7). A thermodynamic path for near isothermal rapid depressurization, such as experienced during isentropic expansion of a subcooled liquid, is illustrated starting at point A and ending at point B. For small depressurization rates, the amount of pressure-undershoot before nucleation occurs is small and flashing occurs near the saturation pressure. As the depressurization rate increases, the amount of pressure-undershoot also increases and flashing occurs at pressures further below the saturation pressure. At an extremely high depressurization rate, the amount of pressure-undershoot is limited by the spinodal pressure. Note that as the nozzle inlet temperature (point A) approach the thermodynamic critical temperature, the spinodal curve approaches the vapor pressure curve and thus decreases the maximum amount of pressure-undershoot. These observations are important for non-equilibrium liquid flow because, for a fixed inlet pressure, as the undershoot pressure decreases, the pressure differential to drive the flow increases and thus the flow rate also increases. This phenomenon is important for the design and evaluation of pressure relief devices and associated downstream equipment.

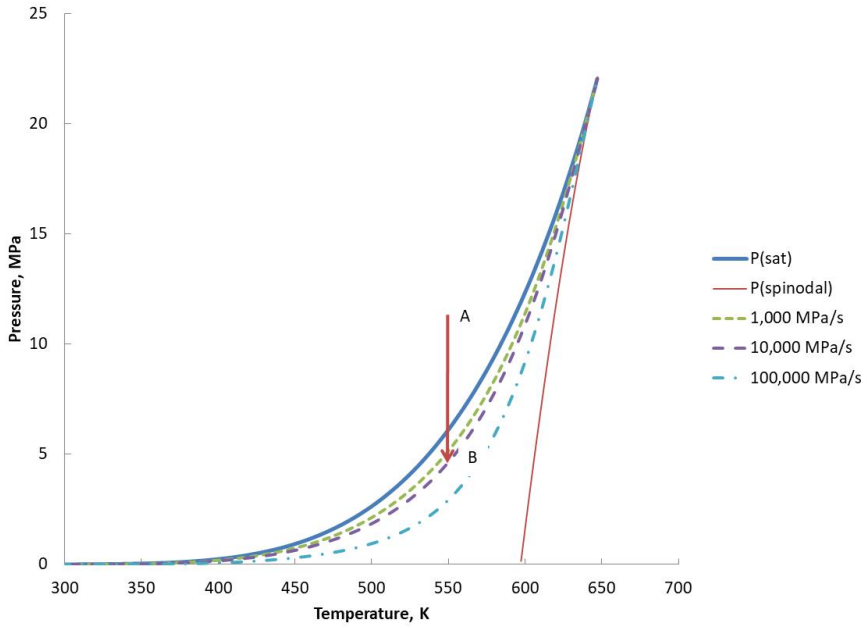

Figure 10.1, Water Depressurization Diagram

Given an undershoot pressure equal to the nozzle throat pressure, Equation 10.1 is used to calculate a Burnell C factor for use in Equations 4.1.1 or 4.1.2.

$$C = 1 - \frac{P_u}{P_s} \tag{10.1}$$

Figure 10.2 illustrates the Burnell C factor diagram for saturated water developed from the Alamgir and Lienhard correlation (Equation 7.7) and Equation 10.1. Comparison of Figure 10.2 with the Weisman and Tentner (1978) correlation (Figure 4.4) shows the Weisman and Tenter correlation fits between the curves for 1,000 and 10,000 MPa/s (0.01 and 0.1 Matm/s).

It is very important to distinguish between the undershoot pressure as estimated from the Alamgir and Lienhard correlation and the flashing pressure at the nozzle throat as is discussed later in the analysis of the Sozzi and Sutherland (1975) data. The pressure-undershoot value estimated using the Alamgir and Lienhard correlation represents the maximum possible departure from equilibrium. The minimum possible departure from equilibrium is of course zero, *i.e.*, flashing at the fluid vapor pressure. The pressure at which flashing occurs at the nozzle throat is between these two extremes and is determined by the fluid initial conditions and the nozzle geometry. Before the data analysis though, scaling to develop depressurization diagrams for chemicals other than water is discussed.

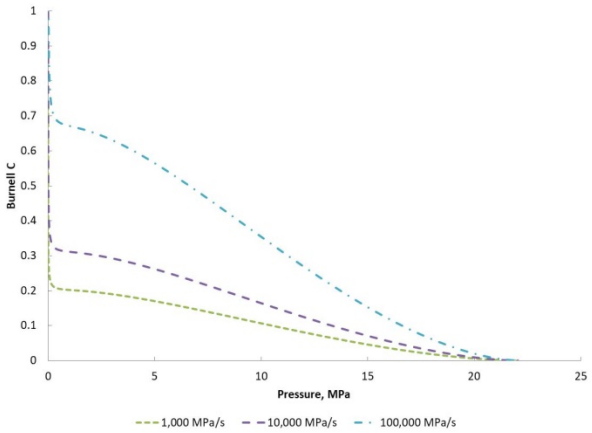

Figure 10.2a, Burnell C – Pressure Diagram

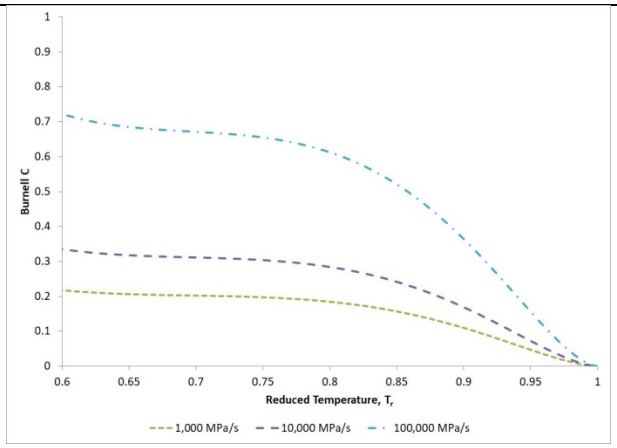

Figure 10.2b, Burnell C – Reduced Temperature Diagram

Figure 10.2, Water Burnell C Factor Diagrams

The nucleation rate is expressed (Brennen, 1995, Equation 1.8) in the general form

$$J = J_0 \exp(-Gb) \tag{10.2}$$

As previously mentioned, Alamgir and Lienhard (1981) used a *Gb*=28.2 for water and pointed out this value represents "real", not homogeneous" nucleation. Water is known to exhibit nucleation rates higher than those for other chemicals, such as hydrocarbons and chlorofluorocarbons. For example, data from Avedisian (1985) indicates that at the thermodynamic stability limit at atmospheric pressure, the water nucleation rate is $9x10^{28}$ nuclei/cm^{3}s while those for n-pentane, n-heptane and n-octane are $8x10^{24}$, $8x10^{26}$, and $2x10^{26}$ nuclei/cm^{3}s, respectively. Brennen (1995) showed that *Gb*=11.5 fits the limit of homogeneous superheat for five liquids (n-pentane, n-hexane, n-heptane, diethyl ether, and benzene) and pointed out the exception to the rule is water. This suggests that the Gibb's number should be different for each type of species.

It is also known that in general, the spinodal curve originates at the thermodynamic critical point and is equal to atmospheric pressure at a reduced temperature, T_r, equal to about 0.9. This suggests that scaling the Gibb's number for chemicals other than water can be done at T_r=0.9.

$$Gb = Gb_w \left(\frac{\sigma}{\sigma_w}\right)^3 \frac{T_{c,w}}{T_c} \left[\frac{(P_{s,w} - P_a)}{(P_s - P_a)} \frac{\left(1 - \frac{\rho_{g,w}}{\rho_{f,w}}\right)}{\left(1 - \frac{\rho_g}{\rho_f}\right)} \right]^2 \Bigg|_{T_r = 0.9} \tag{10.3}$$

Equation 10.3 is derived from equations 7.4 and 7.5, with specific volume replaced by 1/density. In Equation 10.3, the saturation pressures and mass densities at saturation are evaluated at T_r=0.9. The surface tension of both the chemical and water should be evaluated at the normal boiling point temperature of the chemical or the bubble point temperature of a mixture. If the normal boiling point of the chemical is below the freezing point of water, the surface tension ratio should be evaluated at 298.15 K. For example, the R-11 boiling point temperature 296.92 K, the critical temperature is 471.06 K and the estimated Gibb's number is 14.13. As a result, the constant in Equation 7.7 is changed from 0.252 to 0.354. The resulting R-11 depressurization and Burnell C factor diagrams are illustrated in Figures 10.3 and 10.4, respectively.

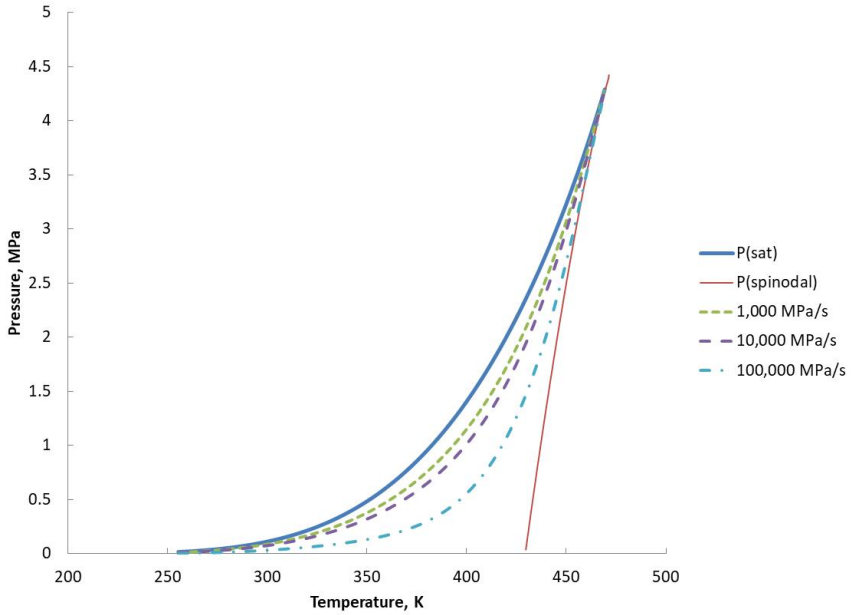

Figure 10.3, R-11 Depressurization Diagram

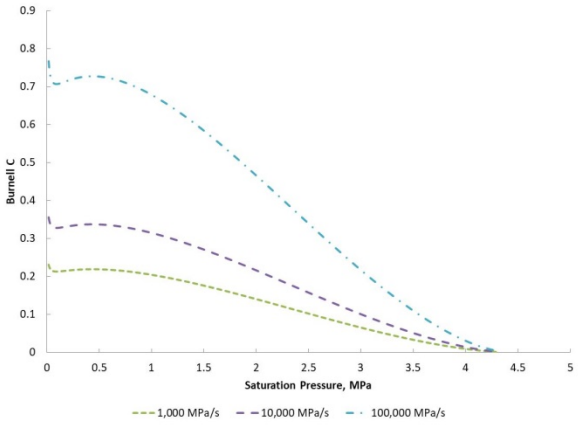

Figure 10.4a, Burnell C – Pressure Diagram

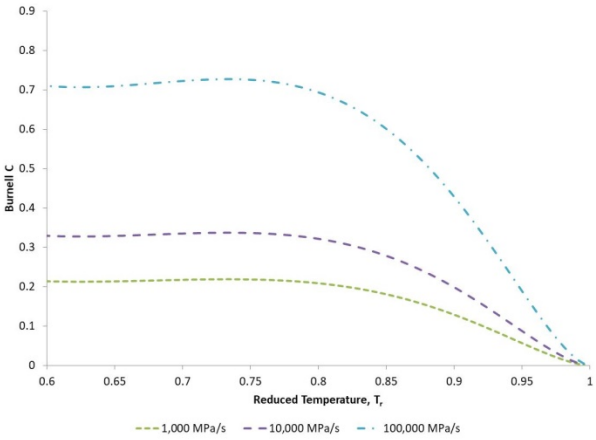

Figure 10.4b, Burnell C – Reduced Temperature Diagram

Figure 10.4, R-11 Burnell C Factor Diagrams

Because of the Gibbs number scaling, and the form of the Alamgir-Lienhard correlation, the Burnell C – Reduced Temperature Diagrams for various chemical species can be combined, as shown in Figure 10.5. It is notable that the Burnell C factors are approximately equal for a given reduced temperature and depressurization rate.

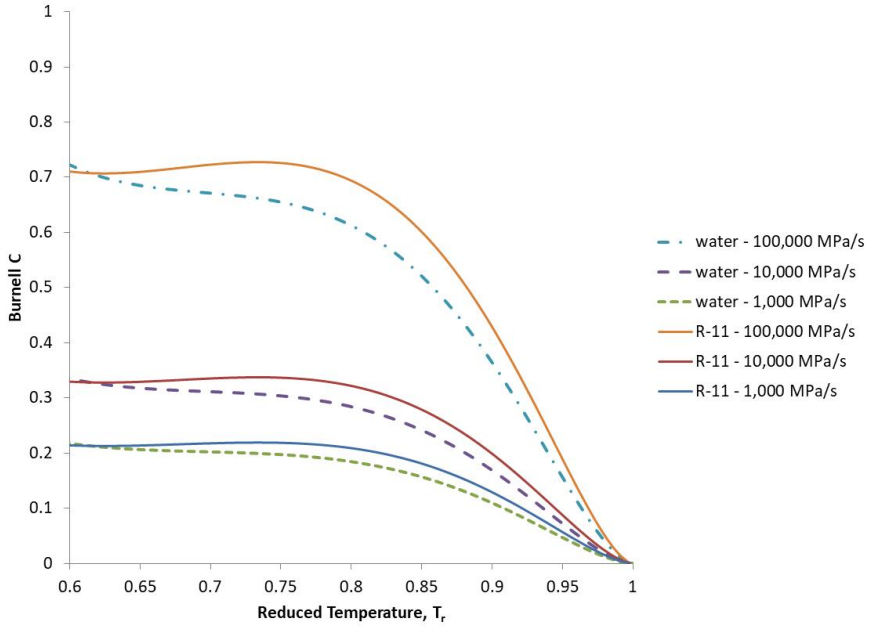

Figure 10.5, Combined Burnell C Diagram

11. Data Analysis

Analyses of nozzle flow data for water from Sozzi and Sutherland (1975) and for R-11 from Prisco (1975) are presented in this section. The described methods provide reasonable agreement with measured data sets.

11.1 Sozzi and Sutherland (1975) Water-Steam Data

Sozzi and Sutherland (1975) conducted a series of blowdown experiments to measure the critical flow rate of water through various nozzles. The experiments included subcooled, saturated and two-phase flow entering the nozzles. The data analysis herein is only applicable to subcooled or saturated liquid nozzle inlet flows.

The Sozzi and Sutherland experiments were performed by discharging high pressure water from a vessel to atmosphere through various nozzles. The nozzles were mounted with the entrance to the nozzle flush with the inside wall of the blowdown vessel to minimize irreversible pressure losses of the fluid as it accelerated from the stagnation condition to the minimum cross-sectional area of the nozzles. Sozzi and Sutherland's "nozzle 2" was chosen for this analysis (Figure 11.1.1). Note in the Sozzi and Sutherland terminology, the "length" of the nozzle refers to the length of the straight section downstream of the converging section. For example, a "zero" length nozzle does not actually have zero length; the actual length is the converging section length.

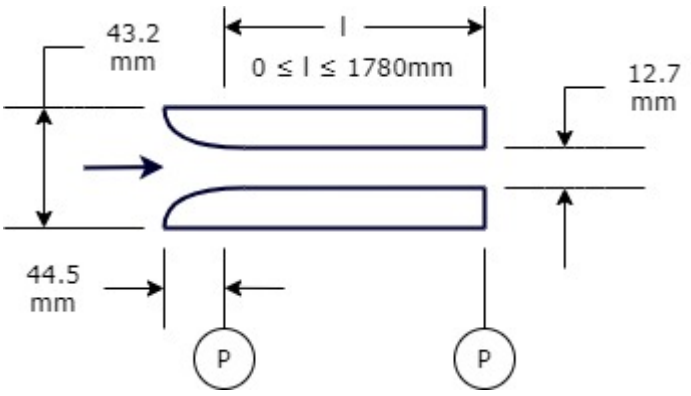

Figure 11.1.1, Sozzi and Sutherland (1975) Nozzle 2 with Length of Straight Tube

It has been suggested that equilibrium flow can be assumed for nozzle lengths greater than 100 mm (4 inches). To test this hypothesis, the throat pressures calculated using the Burnell equation (Equation 4.1.2) were compared to the saturation pressures. In Figure 11.1.2, both the calculated throat pressures and the saturation pressures have been normalized relative to the inlet pressures. While it is true that the throat pressures approach the saturation pressures as the nozzle length increases, there is deviation from equilibrium for the 114.3 mm (4.5 inches) and longer nozzles. The amount of deviation depends on the amount of feed subcooling. *Since approach to equilibrium is a time-based phenomenon, a residence time criterion is recommended rather than a length criterion.* Note that the calculated throat pressures are higher than the saturation pressures for three points. It is proposed that this is due to experimental error but the measured nozzle throat pressures were not provided to validate this hypothesis.

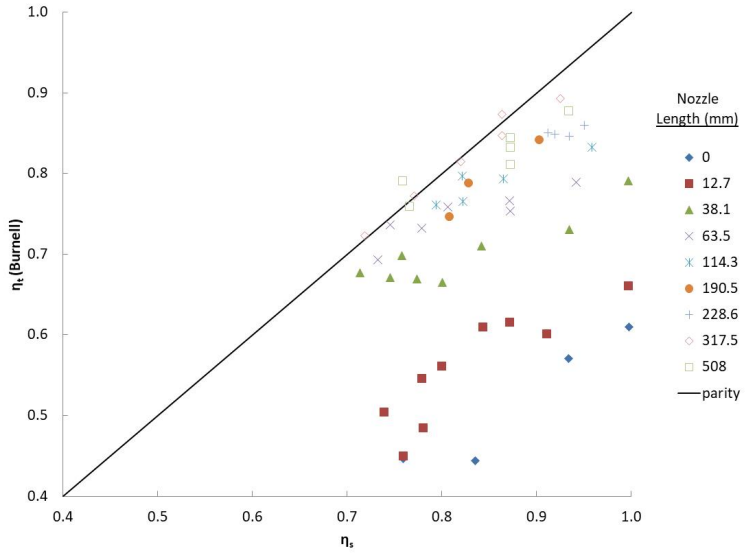

Figure 11.1.2, Comparison of Normalized Saturation Pressures with Normalized Throat Pressures Calculated using the Burnell Equation

The throat pressures calculated using the Burnell equation were also compared to the bubble nucleation pressures as estimated by the Alamgir and Lienhard correlation (Equation 7.7). The shape of the converging section is required in order to calculate the depressurization rate, but it was not specified in the Sozzi and Sutherland article. It was, however, described as a “rounded inlet,” as depicted in Figure

11.1.1. For convenience, it was assumed the shape of the nozzle inlet could be represented by a sine function. The depressurization rate associated with steady-state acceleration of an incompressible fluid was then calculated as follows. The nomenclature is illustrated in Figure 11.1.3.

$$h = h_0 sin\left(\frac{\pi z}{2L}\right) \tag{11.1.1}$$

$$d_c = D - 2h_0 sin\left(\frac{\pi z}{2L}\right) \tag{11.1.2}$$

$$A = \frac{\pi}{4}\left[D - 2h_0 sin\left(\frac{\pi z}{2L}\right)\right]^2 \tag{11.1.3}$$

$$u = \frac{\dot{m}}{\rho A} = \frac{dz}{dt} \tag{11.1.4}$$

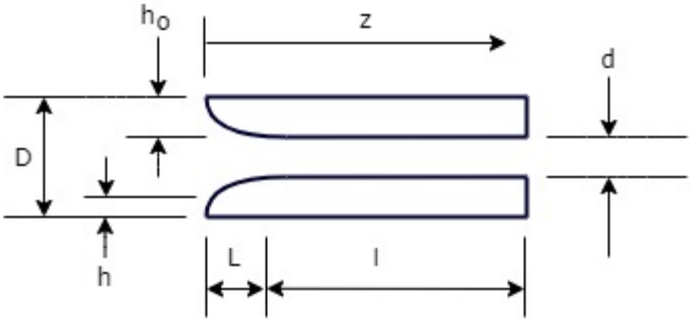

Figure 11.1.3, Nomenclature Applied to Sozzi and Sutherland (1975) Nozzle 2

The Sozzi and Sutherland nozzle 2 dimensions are D=43.2 mm, d=12.7 mm, h_0=15.25 mm and L=44.5 mm. Upon rearranging and integrating the velocity equation, Equation 11.1.4, from time = 0 to t and z = 0 to L, the residence time in the converging section is found to be

$$\tau = \frac{\rho}{\dot{m}}\frac{\pi}{4}\int_0^L \left[D - 2h_0 sin\left(\frac{\pi z}{2L}\right)\right]^2 dz \tag{11.1.5}$$

$$\tau = \frac{\rho L}{\dot{m}}\left(\frac{\pi}{4}D^2 + \frac{\pi}{2}h_0^2 - 2Dh_0\right) \tag{11.1.6}$$

The acceleration pressure drop of the yet non-flashing incompressible liquid flow in the converging section is calculated using the steady-state differential mechanical energy balance (Equation 4.1)

$$-\frac{dP}{dz} = \rho u \frac{du}{dz} \tag{11.1.7}$$

Upon combination with the incompressible continuity equation ($\frac{du}{u} = -\frac{dA}{A}$) and multiplication by the velocity, Equation 11.1.7 becomes

$$\frac{dP}{dt} = u\frac{dP}{dz} = \frac{\rho u^3}{A}\frac{dA}{dz} = \frac{\dot{m}^3}{\rho^2 A^4}\frac{dA}{dz} \tag{11.1.8}$$

Equation 11.1.8 is equivalent to Equation 7.11 with the transient component equal to zero. From Equation 11.1.3, the derivative of the area is

$$\frac{dA}{dz} = -\frac{\pi^2 h_0}{2L}\left[D - 2h_0 sin\left(\frac{\pi z}{2L}\right)\right] cos\left(\frac{\pi z}{2L}\right) \tag{11.1.9}$$

The final relationship between the depressurization rate and nozzle geometry is obtained by combining Equations 11.1.8 and 11.1.9.

$$\frac{dP}{dt} = -\frac{\dot{m}^3}{\rho^2 A^4}\frac{\pi^2 h_0}{2L}\left[D - 2h_0 sin\left(\frac{\pi z}{2L}\right)\right] cos\left(\frac{\pi z}{2L}\right) \tag{11.1.10}$$

The depressurization rate to use in the Alamgir and Lienhard correlation, Equation 7.7, is found by determining the maximum depressurization rate given by Equation 11.1.10. The maximum depressurization rate determines the lower bound on the throat pressure. The location of the maximum depressurization rate is obtained by differentiating Equation 11.1.10 with respect to z and setting that result equal to zero to obtain Equation 11.1.11. The location of the maximum depressurization rate is obtained by solving Equation 11.1.11 for z.

$$D - 2h_0 sin\left(\frac{\pi z}{2L}\right) = 14 h_0 cos\left(\frac{\pi z}{2L}\right) cot\left(\frac{\pi z}{2L}\right) \tag{11.1.11}$$

For the Sozzi and Sutherland nozzle 2 geometry, the location of the maximum depressurization rate is found to occur at z = 37.656 mm (1.471 inches). The depressurization rate at that location is found using Equations 11.1.10 and 11.1.12 and then used in the Alamgir and Lienhard correlation to estimate the pressure-undershoot.

$$\Sigma' = \left(-\frac{dP}{dt}\right)_{max} \tag{11.1.12}$$

An example depressurization rate calculation result is illustrated in Figure 11.1.4. The distance on the abscissa is from the nozzle entrance to the end of the converging section. One can see in the illustration the peak depressurization rate occurs over a short distance in the nozzle converging section.

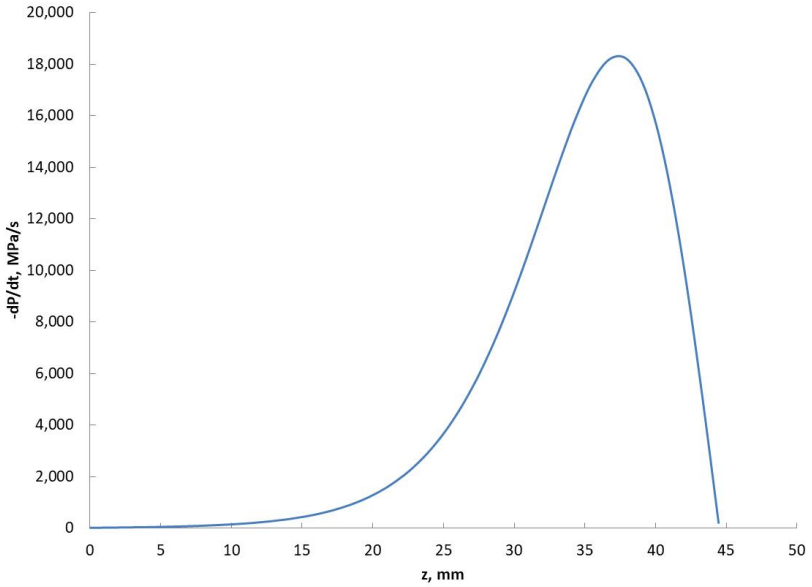

Figure 11.1.4, Example Calculated Water Depressurization Rate for Sozzi and Sutherland (1975) Nozzle 2 for l=0 mm (0 inches)

The normalized nozzle throat pressure calculated with the Burnell equation is related to the converging section maximum depressurization rate in Figure 11.1.5. Deviation from a smooth curve for longer nozzles and smaller depressurization rates occurs because friction losses in the straight section of the nozzles become more important. One can also note that fluids flowing through longer nozzles experience larger residence times and flashing may commence before the nozzle throat. The method described in this article only applies when rapid flashing occurs essentially at the nozzle throat.

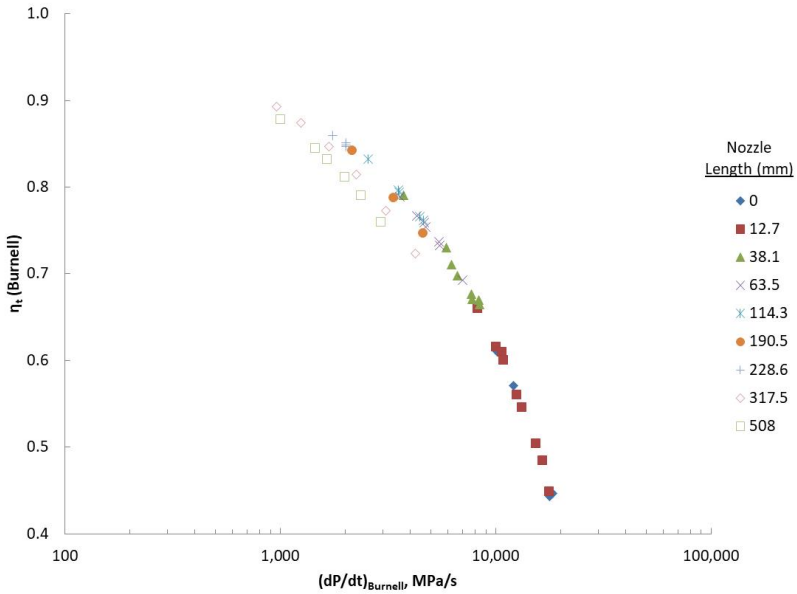

Figure 11.1.5, Normalized Nozzle Throat Pressures for Sozzi and Sutherland (1975) Nozzle 2

The throat pressures calculated using the Burnell equation for the various nozzle lengths were overlaid on the water depressurization diagram (Figure 11.1.6). One can see the general trend is as expected.

More detailed comparisons for l=0 mm (0 inches) and l=12.7 mm (0.5 inches) are illustrated in Figures 11.1.7 and 11.1.8. The agreement between the bubble nucleation method and the Burnell method indicates acceleration losses are a major contributor to the amount of fluid superheat, i.e., metastability. However, for longer nozzle lengths a more detailed investigation reveals another phenomenon that must be considered.

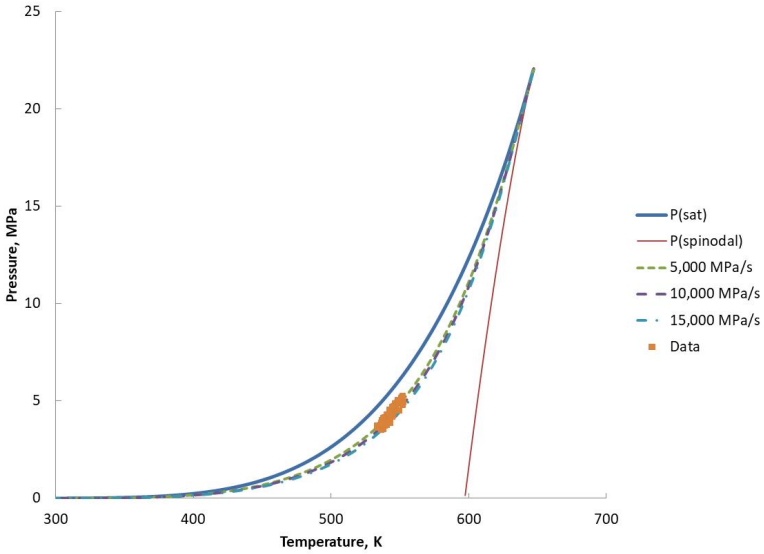

Figure 11.1.6, Sozzi and Sutherland (1975) Water Depressurization Diagram

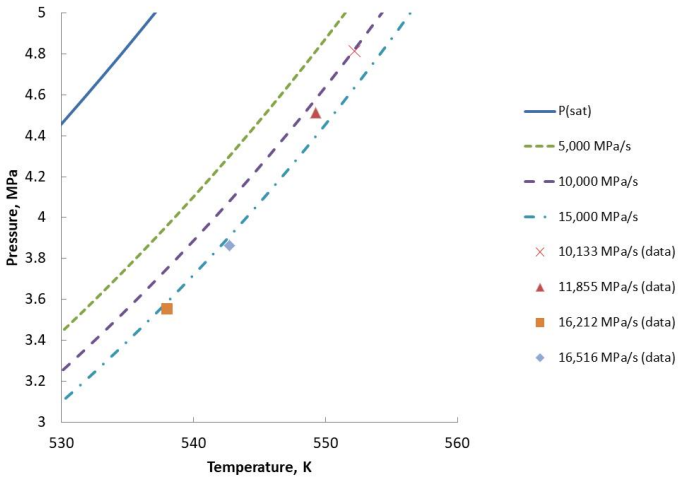

Figure 11.1.7, Sozzi and Sutherland (1975) Depressurization Diagram for l=0 mm (0 inches)

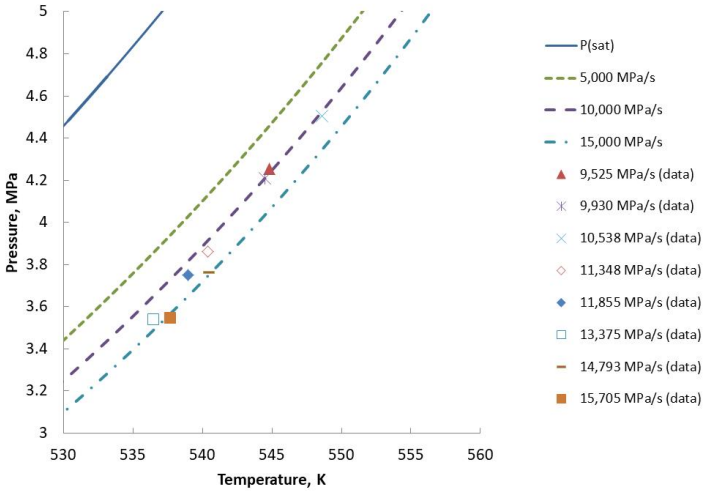

Figure 11.1.8, Sozzi and Sutherland (1975) Depressurization Diagram for l=12.7 mm (0.5 inches)

Figure 11.1.9 depicts the combined effects of initial subcooling and depressurization rates on the resulting deviation from equilibrium at the nozzle exit. The results are illustrated for the 114.3 mm (4.5 inches) long nozzle. The 114.3 mm nozzle length data was selected to demonstrate that non-equilibrium conditions can still occur at the exit of nozzles greater than 100 mm in length. For small depressurization rates or for large degrees of initial subcooling, the bubble nucleation pressures, and thus the nozzle throat pressures, approach the fluid saturation pressures; namely, the Burnell C factors approach zero. For large depressurization rates or for small degrees of initial subcooling, the bubble nucleation pressures, and thus the nozzle throat pressures, approach the bubble nucleation pressures predicted by the Alamgir and Lienhard correlation. The reasons for these phenomena are illustrated in Figure 11.1.9.

In Figure 11.1.9a, the depressurization rate is small (ca. 2,500 MPa/s), compared to that in Figures 11.1.9b and c (ca. 3,500 MPa/s) as indicated by the peak depressurization rate located at z = 37.656 mm. The amount of initial subcooling is also small as indicated by the small difference between the saturation pressure and the nozzle inlet pressure at the nozzle inlet (z=0). The local fluid pressure decreases due to acceleration as it flows through the nozzle converging section, as indicated by the solid line. The nozzle throat pressure approaches the Alamgir and Lienhard nucleation pressure, P_n, because the local pressure is smaller than the vapor pressure when the fluid has reached its maximum depressurization rate. Thus, in the case of shorter nozzles with larger peak depressurization rates, the nozzle throat pressures approach the Alamgir and Lienhard nucleation pressure.

Figure 11.1.9c represents the opposite extreme of a large amount of subcooling with a large peak depressurization rate. For this case, because of the large degree of initial subcooling, the local pressure is still larger than the fluid vapor pressure at the location of maximum depressurization rate. Consequently, in this case, the nucleation pressure at the nozzle throat approaches the fluid vapor pressure.

Figure 11.1.9b illustrates an intermediate case where the depressurization rate is large and the local pressure at the location of maximum depressurization rate is near the fluid vapor pressure. In this case the flashing pressure at the nozzle throat is between the two extremes. *As illustrated, the Alamgir and*

Lienhard nucleation pressure can be considered the maximum potential amount of non-equilibrium given enough pressure driving force to cause it to occur.

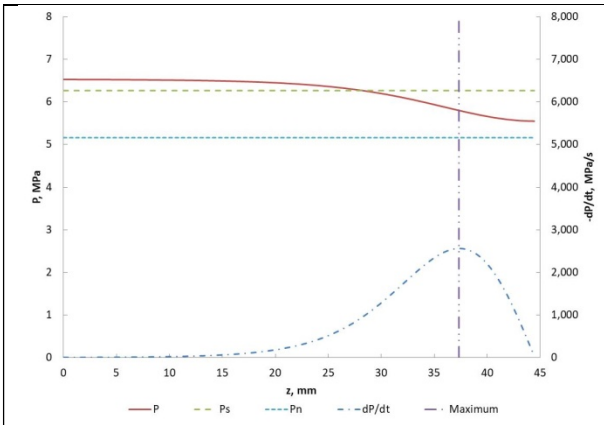

Figure 11.1.9a, Large Pressure-undershoot

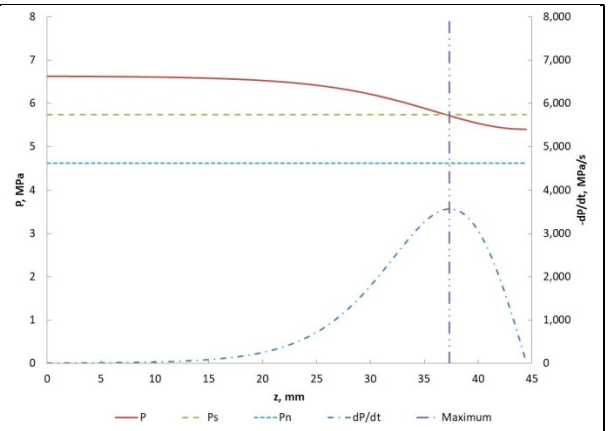

Figure 11.1.9b, Intermediate Pressure-undershoot

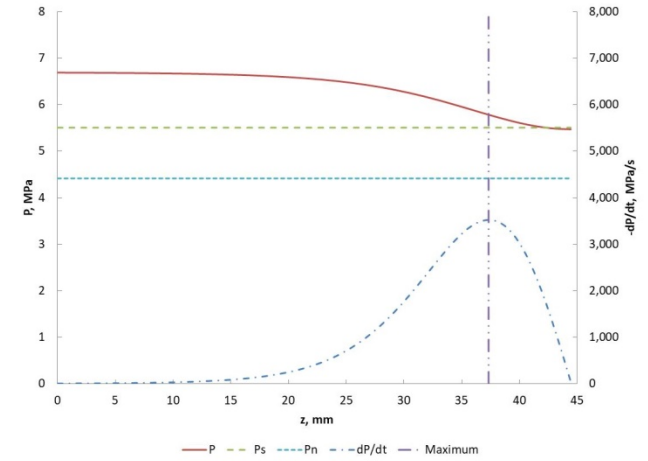

Figure 11.1.9c, Minimum Pressure-undershoot

Figure 11.1.9, Pressure-undershoot at Point of Maximum Acceleration for l=114.3 mm (4.5 inches)

The non-equilibrium phenomena shown in Figure 11.1.9 can be quantified by defining an "efficiency" to adjust the pressure-undershoot determined by the Alamgir and Lienhard correlation. The "driving force" for non-equilibrium is the difference between the fluid saturation pressure and the local pressure at the location of the maximum depressurization rate. The "efficiency" can be thought of as an approach to equilibrium.

$$(P_{sat} - P_{n,relaxed}) = \eta(P_{sat} - P_{n,A-L}) \tag{11.1.13}$$

The nucleation pressure calculated using the Alamgir and Lienhard correlation is adjusted with the approach to equilibrium "efficiency" to determine the nozzle throat pressure, $P_{n,relaxed}$. The nozzle throat pressure is then used in Equation 11.1.14 to estimate the mass flux.

$$G = \sqrt{\frac{2\rho_0\left(P_0 - P_{n,relaxed}\right)}{1+f_D\frac{l}{d}}} \qquad (11.1.14)$$

In practice a trial-and-error solution is required because the maximum depressurization rate and the local pressure at the location of the maximum depressurization rate are not known *a priori*. The calculation method is described and an example calculation is provided in Appendix B.

The approach to equilibrium efficiency is depicted as a function of the "driving force" for nucleation in Figure 11.1.10. A solid line is drawn at an efficiency of one to indicate values larger than one are not used. The reasons for values greater than one obtained during the data analysis are described in the next paragraph.

The premise for the use of the Bernoulli or Burnell equations to estimate nozzle critical flow is that rapid flashing occurs predominately near the nozzle exit. The difference between the two equations is that boiling is "delayed" below the saturation pressure when using the Burnell equation. A nucleation delay time of 1 millisecond has been reported (see for example Sozzi and Sutherland (1975) "Discussion of Results"). With a 1 millisecond nucleation delay time, flashing almost certainly occurs downstream of the Sozzi and Sutherland "zero" length nozzle and likely also occurs downstream of the 12.7 mm (0.5 inch) long nozzle. The residence time in the straight section of the 12.7 mm (0.5 inch) long nozzle is 0.14 – 0.17 milliseconds assuming all liquid flow. The transition between flashing downstream of the nozzle and flashing in the nozzle likely occurs in the 38.1 mm (1.5 inches) long nozzle, with flashing possibly occurring downstream of the nozzle for the most subcooled data points and within the nozzle for the least subcooled data points. The data points in Figure 11.1.10 having efficiencies greater than one are for the shortest nozzles where flashing is likely occurring downstream of the nozzles and are thus not applicable for the current model premise.

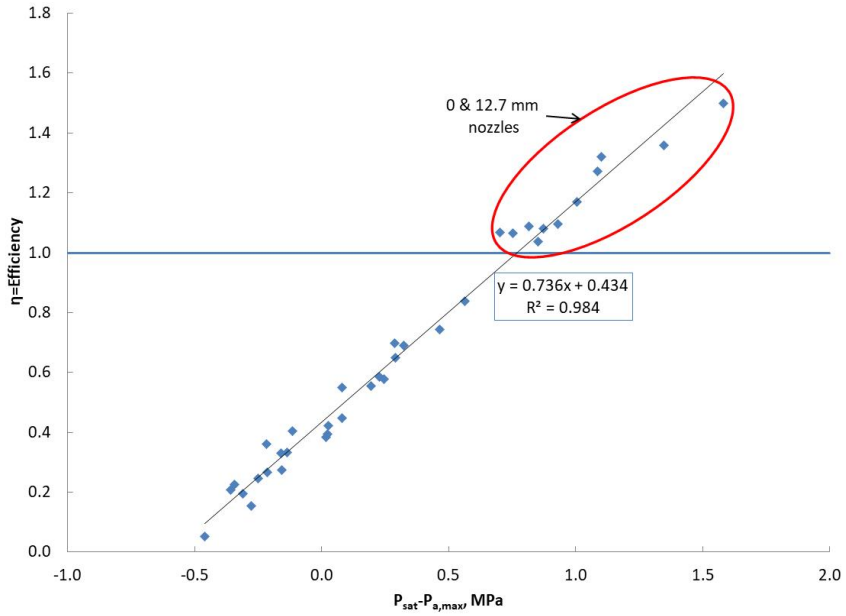

Figure 11.1.10, Efficiency of Converting Potential Bubble Nucleation Pressure to Nozzle Throat Pressure

The nozzle throat pressures were not generally provided in the Sozzi and Sutherland (1975) data so the nozzle throat pressure calculated using Equation 11.1.13 (notated as $P_{nucleation}$ to represent use of the nucleation theory) is compared to the nozzle throat pressure using the Burnell equation in Figure 11.1.11. The agreement is generally acceptable. To be clear, experimental values of the stagnation pressure and mass flux were used in Equation 4.1.2 to calculate the Burnell C factor and the "Burnell" throat pressure along with the equation $P_t = (1 - C)P_s$. Disagreement between the two calculation methods occurs for the two shortest nozzles (0 and 12.7mm) when flashing takes place downstream of the nozzle.

Two comparisons of the mass fluxes calculated using the bubble nucleation method and the experimental data are found in Figure 11.1.12. Again the bubble nucleation method provides generally good agreement with the measured data except for the shortest nozzles. Calculation of the Burnell C factor is straightforward given the nozzle throat pressure. The Burnell C factor calculated using the nucleation theory is compared to that calculated using the Burnell equation in Figure 11.1.13. Again, when choking is concurrent with flashing at the nozzle throat, the two methods agree. The exceptions are when choking occurs downstream of the nozzle throat in the two shortest nozzles.

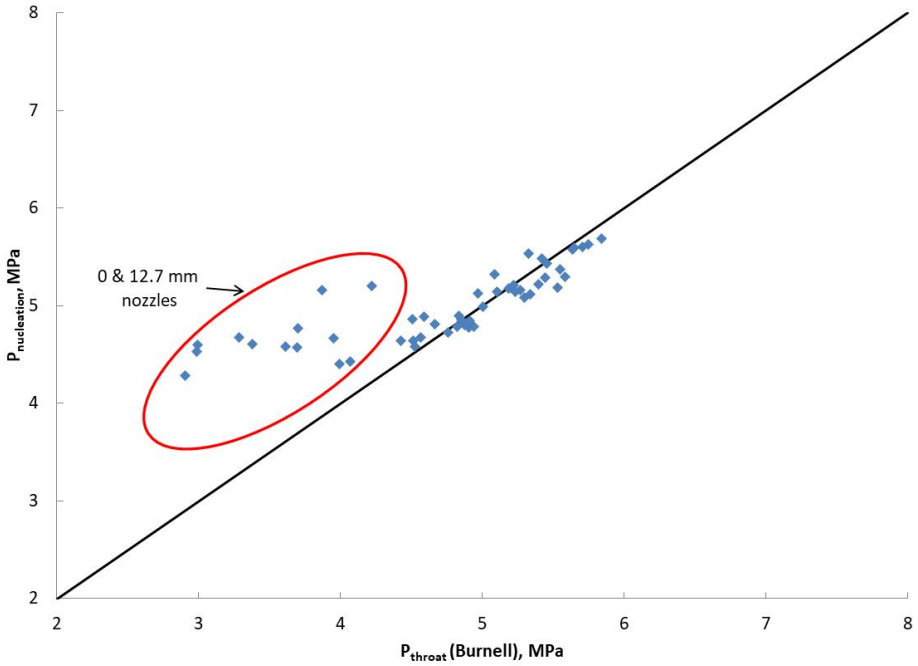

Figure 11.1.11, Sozzi and Sutherland (1975) Nozzle 2 Outlet Pressures

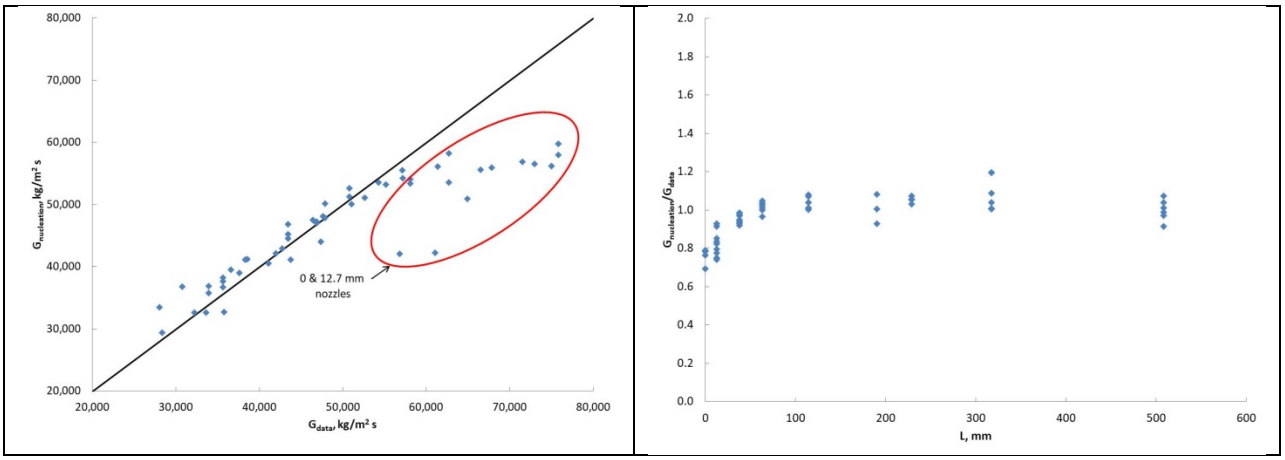

Figure 11.1.12, Sozzi and Sutherland (1975) Nozzle 2 Mass Fluxes

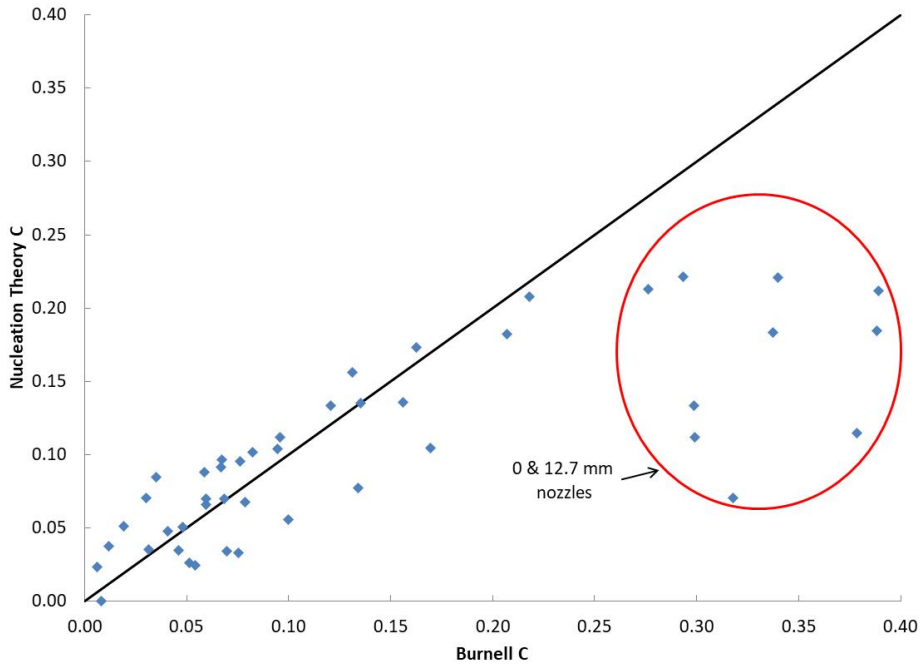

Figure 11.1.13, Sozzi and Sutherland (1975) Nozzle 2 Burnell C Factor

11.2 Prisco (1975) R-11 Data

Prisco (1975) studied the flow of R-11 (CCl_3F) through nozzles with sharp-edged entrances. Data from two geometries are considered herein. The first geometry is a nozzle with a constant-diameter portion followed by a 7° diverging exit cone (Figure 11.2.1), referred to as Nozzle C7. A face cut was taken across the inlet flange and nozzle entrance on a lathe to ensure a sharp-edged entrance. The inside surface of the upstream constant-diameter portion was polished with emery paper. The nozzle inside diameter is 8 mm (0.313 inch) and data was collected for three length-to-diameter ratios: 12.78, 7.96 and 2.82. The length of the constant-diameter portion of the nozzles was varied to achieve the reported length-to-diameter ratios. The nozzle inlet flange was connected to a 50.8 mm (2 inch) diameter port located on the R-11 supply vessel, resulting in a beta ratio for the sudden contraction of about 0.16.

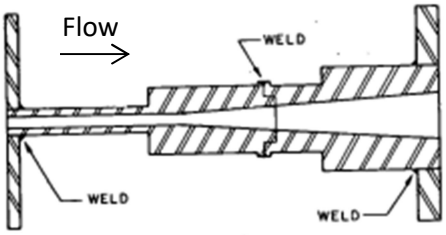

Figure 11.2.1, Nozzle C7 (from Prisco, 1975)

The second nozzle considered is referred to as Nozzle C120. This nozzle has a constant-diameter portion followed by a 120° diverging exit cone. The diverging cone is followed by a second constant-diameter section (Figure 11.2.2). As with Nozzle C7, a face cut was taken across the inlet flange and nozzle entrance on a lathe to ensure a sharp-edged entrance and the inside surface of the upstream constant-diameter portion was polished with emery paper. The nozzle inside diameter is 8 mm (0.313 inch) and data was collected for three length-to-diameter ratios: 12.78, 7.97 and 2.82. The length of the upstream constant-diameter portion of the nozzles was varied to achieve the reported length-to-diameter ratios. The nozzle inlet flange was connected to a 50.8 mm (2 inch) diameter port located on the R-11 supply vessel, resulting in a beta ratio for the sudden contraction of about 0.16.

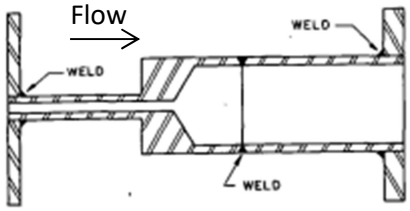

Figure 11.2.2, Nozzle C120 (from Prisco, 1975)

In the case of sharp-edged nozzles, and other configurations in which a *vena contracta* is formed, the fluid state throughout the entire flow path must be considered for saturated and slightly subcooled liquid flow into the nozzle. Three cases arise due to the *vena contracta*, depending upon the local pressure relative to the fluid vapor pressure at the minimum pressure location (at the *vena contracta*) and after pressure recovery (downstream of the *vena contracta*). Figure 11.2.3 provides a plot of pressure versus location for flow in a sharp-edged nozzle for equilibrium flow. As a matter of clarity, the term “separation point” designates where fluid streamlines separate from the duct wall upstream of the contraction plane and “detachment” designates fluid separation at the contraction plane. A horizontal dashed line is shown representing the local vapor pressure of the fluid. Three cases typically presented for equilibrium flow are illustrated. For non-equilibrium flow, the bubble nucleation pressure is an additional consideration. If the fluid pressure remains above the vapor pressure for the entire flow path, then Bernoulli flow applies (Figure 11.2.3, case a). If no flashing occurs along the flow path, then the smallest cross-sectional area for flow occurs at the *vena contracta*. The flow rate through the nozzle can thus be estimated using the upstream pressure, *vena contracta* pressure, and *vena contracta* flow area in the Bernoulli equation.

The second case to be considered is cavitating flow (Figure 11.2.3, case b). In this case, the pressure at the *vena contracta* drops below the vapor pressure, but the pressure recovery returns the fluid pressure to a value greater than the vapor pressure. The central liquid core in the separation zone is surrounded by a vapor cloud and flashing in the liquid core occurs in a cavitation region where the local pressure is less than the vapor pressure. Ferrari (2017) reports observations of bubbly flow and bubble foam

patterns during incipient cavitation stages independent of nozzle geometry. As the amount of cavitation increases, the presence of long strips of vapor and vapor films have been observed that do depend on the nozzle geometry. Upon pressure recovery, after the *vena contracta*, rapid collapse of the cavitation pockets can occur. Depending upon the extent of cavitation, instability can occur in which periodic vapor cloud formation and shedding occurs.

The final case to be considered is flashing flow (Figure 11.2.3, case c). In this case, the pressure at the *vena contracta* drops below the vapor pressure and even after pressure recovery, the fluid pressure remains below the vapor pressure. To further complicate the matter, Ferrari (2017) reports that the fluid reattachment point downstream of the *vena contracta* can move instantly to the nozzle exit once the length of the vapor cavity surrounding the liquid jet reaches about 25-35% of the nozzle length. When the vapor cavity length exceeds the nozzle length, and the nozzle outflow is into a vapor, the liquid core is unable to reattach to the nozzle wall. When this occurs, the liquid jet exits the nozzle into the downstream environment without pressure recovery. Ferrari (2017) refers to this condition as a "hydraulic flip". The hydraulic flip is characterized by a sudden reduction in friction losses because there is no contact between the flowing liquid and the nozzle walls. He also reports no hydraulic flip occurs for $L/D \geq 8$ while it does occur at $L/D = 4$. Figure 11.2.3, case c is the pressure profile typically associated with pressure relief valve nozzle analysis where choking is assumed to occur at the nozzle throat, e.g., the HEM applies.

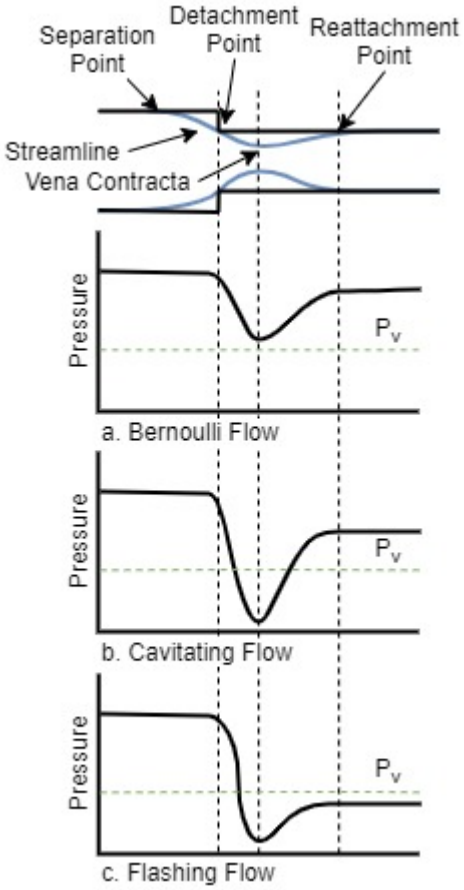

Figure 11.2.3, Fluid Flow Path Considerations for a *Vena Contracta* with Equilibrium Flow

In the case of non-equilibrium flow, the fluid superheating occurs during the acceleration to the *vena contracta*. If the nozzle length downstream of the *vena contracta* is long enough for fluid reattachment and there is enough residence time for the relaxation phenomena to occur, then choking occurs at the nozzle throat based on the local fluid equilibrium conditions. If not, then non-equilibrium effects influence the nozzle capacity. The immediate question is how to estimate the depressurization rate from acceleration losses in the presence of flow separation. It is proposed that the relevant acceleration losses take place from the fluid detachment point at the nozzle inlet to the *vena contracta*.

Streamlines are known to separate from duct walls and acceleration to occur upstream of the sudden contraction (Figure 11.2.4). The entire streamline path from the upstream separation point past the detachment point at the nozzle contraction plane and into the *vena contracta* is used to estimate the relevant fluid acceleration. Rennels and Hudson (2012) provide a correlation for the jet velocity ratio ($\lambda=u_{vc}/u_1$) as a function of the beta ratio ($\beta=d_2/d_1$), Equation 11.2.1

$$\lambda = 1 + 0.622(1 - 0.215\beta^2 - 0.785\beta^5) \qquad (11.2.1)$$

The jet velocity ratio obtained from Equation 11.2.1 was used to calculate the vena contracta flow area in the Prisco data analysis.

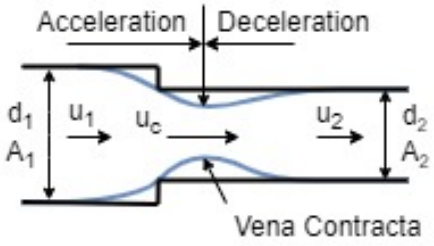

Figure 11.2.4, Streamlines in a Sudden Contraction

Dimensions required for estimating depressurization rates from Bullen (1996) are summarized in Table 11.2.1. The data from Bullen were acquired using an upstream diameter d_1 = D = 110 mm. The downstream diameter (d_2 = d) was varied to achieve the desired area ratios. Given the jet velocity ratio and the relevant nozzle dimensions, what remains to determine is the fluid acceleration rate.

A_2/A_1	0.13-0.67
Reynold's Number	40,000-200,000
Upstream separation point (distance upstream of contraction plane)	1-1.5D
Vena contracta location (distance downstream of contraction plane)	0.225D
Downstream reattachment point (distance downstream of contraction plane)	~0.5D

Table 11.2.1, Dimensions of Detachment and Reattachment Points in Nozzle Flow from Bullen (1996)

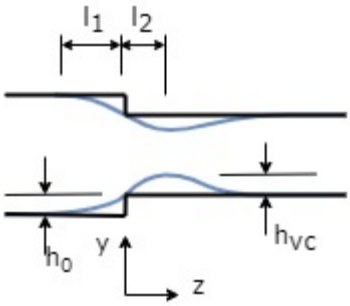

Figure 11.2.5, *Vena Contracta* Calculation Nomenclature

Figure 11.2.5 illustrates the nomenclature used to calculate the *vena contracta* dimensions. The streamline upstream of the contraction plane (z=0) is assumed to be represented by a power law relationship

$$y_u = a_1(z + l_1)^{b_1} \tag{11.2.2}$$

At $z = 0, y_u = h_0,\ \therefore h_0 = a_1(l_1)^{b_1}$

The streamline flow from the contraction plane to the vena contracta is assumed to be represented by a parabola

$$y_d = -a_2(z - l_2)^2 + h_{vc} + h_0 \tag{11.2.3}$$

At $z = 0, y_d = h_0,\ \therefore h_{vc} = a_2(l_2)^2$

Note, with the assumed parabolic shape, the fluid reattachment point is twice the distance from the contraction plane as the *vena contracta*. Requiring the slopes of Equations 11.2.2 and 11.2.3 to be equal at z = 0 for continuity of the two descriptive functions, gives

$$b_1 = \frac{2a_2 l_1 l_2}{h_0} = 2\frac{l_1}{l_2}\frac{h_{vc}}{h_0} \tag{11.2.4}$$

With the stated assumptions, all of the equation constants are specified. The resulting flow areas are

$$A_u = \frac{\pi}{4}[D - 2a_1(z + l_1)^{b_1}]^2 \tag{11.2.5}$$

$$A_d = [(d - 2h_{vc}) + 2a_2(z - l_2)^2]^2 \tag{11.2.6}$$

The residence times before and after the contraction plane are determined by integration of Equation 11.2.7.

$$u = \frac{dz}{dt} = \frac{\dot{m}}{\rho A} \tag{11.2.7}$$

The residence times upstream and downstream of the contraction plane are then

$$\tau_u = \frac{\rho}{\dot{m}}\frac{\pi}{4}\int_{-l_1}^{0}[D - 2a_1(z + l_1)^{b_1}]^2\, dz \tag{11.2.8}$$

$$\tau_u = \frac{\rho}{\dot{m}}\frac{\pi}{4} l_1 \left(D^2 - \frac{4Dh_0}{b_1+1} + \frac{4h_0^2}{2b_1+1}\right) \tag{11.2.9}$$

$$\tau_d = \frac{\rho}{\dot{m}}\frac{\pi}{4}\int_0^{l_2}[(d-2h_{vc})+2a_2(z-l_2)^2]^2\,dz \tag{11.2.10}$$

$$\tau_d = \frac{\rho}{\dot{m}}\frac{\pi}{4}l_2\left[(d-2h_{vc})^2+\frac{4}{3}(d-2h_{vc})h_{vc}+\frac{4}{5}h_{vc}^2\right] \tag{11.2.11}$$

The fluid depressurization rate is determined by Equation 11.1.8, repeated here for convenience

$$\frac{dP}{dt} = u\frac{dP}{dz} = \frac{\rho u^3}{A}\frac{dA}{dz} = \frac{\dot{m}^3}{\rho^2 A^4}\frac{dA}{dz} \tag{11.1.8}$$

The derivatives of the flow areas with respect to distance are given by

$$\frac{dA_u}{dz} = -\pi a_1 b_1[D-2a_1(z+l_1)^{b_1}]\,(z+l_1)^{b_1-1} \tag{11.2.12}$$

$$\frac{dA_d}{dz} = 2\pi a_2[(d-2h_{vc})+2a_2(z-l_2)^2](z-l_2) \tag{11.2.13}$$

Once again, the location of the maximum rate of depressurization is found by differentiating Equation 11.1.8 with respect to distance and setting the result equal to zero. The maximum rate of depressurization is found to be located in the *vena contracta* as given in Equation 11.2.14.

$$z_{a,max} = l_2 - \sqrt{\frac{d-2h_{vc}}{26a_2}} \tag{11.2.14}$$

An example illustrating the depressurization rate calculated using data from Prisco's (1975) Nozzle C120, Run 1-2-1 data is found in Figure 11.2.6. In Prisco's Run 1-2-1, the nozzle length/diameter ratio is 12.78 and the nozzle constant diameter length is 101.6 mm (4 inches). In Figure 11.2.6, the distance on the abscissa is from the fluid streamline separation point upstream of the nozzle contraction plane to the re-expansion of the *vena contracta* downstream of the contraction plane. The contraction plane is located at z = 0. The depressurization rate depends on the beta ratio and the depressurization rate downstream of the contraction plane is larger than the depressurization rate upstream of the contraction plane for a wide range of beta ratios. The magnitude of superheating due to fluid acceleration is thus largely controlled by acceleration from the detachment point at the contraction plane to the *vena contracta*. The result is consistent with Prisco's (1975) conclusion that "the non-equilibrium is caused when the fluid sustains a sudden pressure drop as it passes through the sharp-edged entrance."

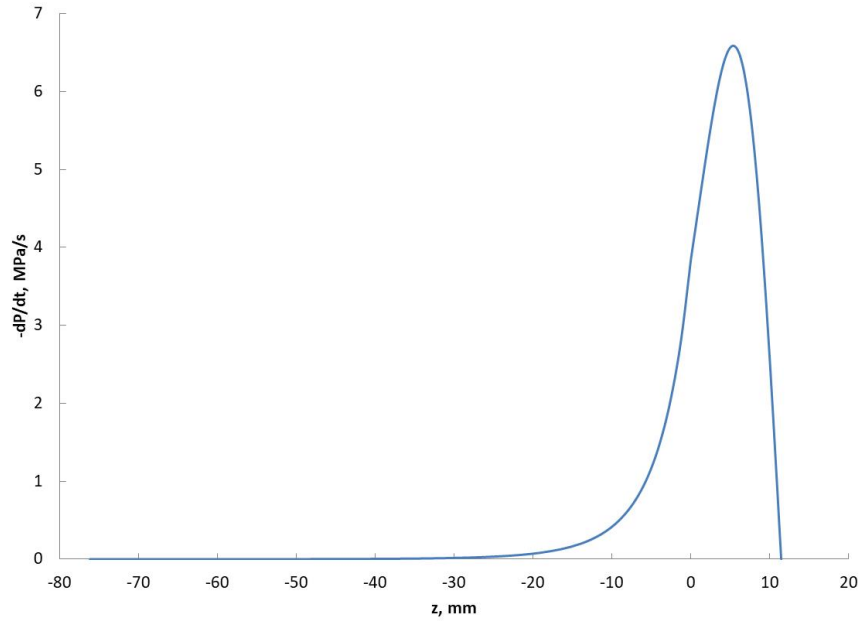

Figure 11.2.6, Example Calculated R-11 Depressurization Rate for Prisco (1975) Nozzle C120, Run 1-2-1

The data from Prisco was analyzed to determine if Bernoulli flow, cavitating flow or flashing flow was occurring. Prisco's experimental procedure included stirring the R-11 with nitrogen while heating or cooling to ensure thermal homogeneity. He then used air pressure to maintain a constant static pressure above the R-11 during the experimental runs. It is safe to say the R-11 was saturated with nitrogen and analysis of the data supports that premise. It is straightforward to calculate the nitrogen partial pressure and thus nitrogen solubility in each run. The mole fraction of nitrogen in the liquid phase ranges from 0.0002 to 0.0008. If equilibrium flow was occurring, clearly nitrogen would come out of solution as the pressure decreased below the stagnation pressure.

The *vena contracta* pressure can be estimated using the Bernoulli equation and by assuming frictionless flow. The calculated *vena contracta* pressures are compared to data Prisco provided along the axial distance of the nozzles in Figure 11.2.7. In Figure 11.2.7, the notation P_{sx} indicates the pressure measured at the pressure tap nearest to the inlet of the nozzle. The agreement between the calculated and measured pressures supports the conclusion that the *vena contracta* pressure is largely determined by pressure losses associated with fluid acceleration. It is also noteworthy that there was essentially no axial pressure drop between the *vena contracta* and the nozzle exit plane indicated in Prisco's data. Example pressure profiles are shown in Figure 11.2.8. The lack of pressure recovery after the *vena contracta* indicates fluid reattachment to the nozzle wall downstream of the *vena contracta* did not occur. These observations support Prisco's conclusions that the flow occurred in a central core consisting of a superheated liquid jet surrounded by a two-phase mixture annulus (Figure 11.2.9).

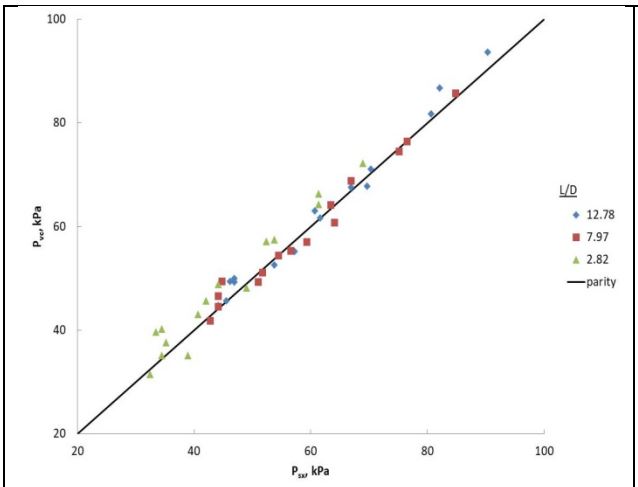

Figure 11.2.7a, Prisco Nozzle C7

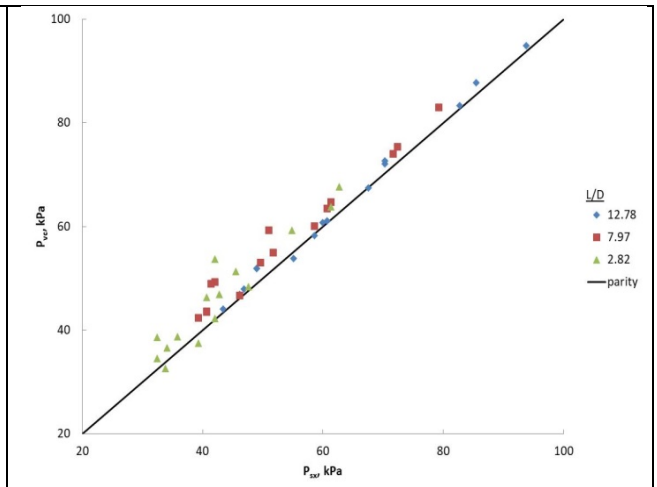

Figure 11.2.7b, Prisco Nozzle C120

Figure 11.2.7, *Vena Contracta* Pressure for Prisco (1975) Nozzles

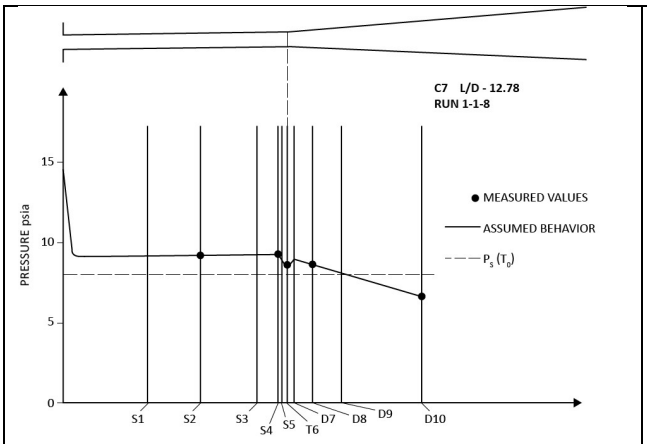

Figure 11.2.8a, Prisco Nozzle C7

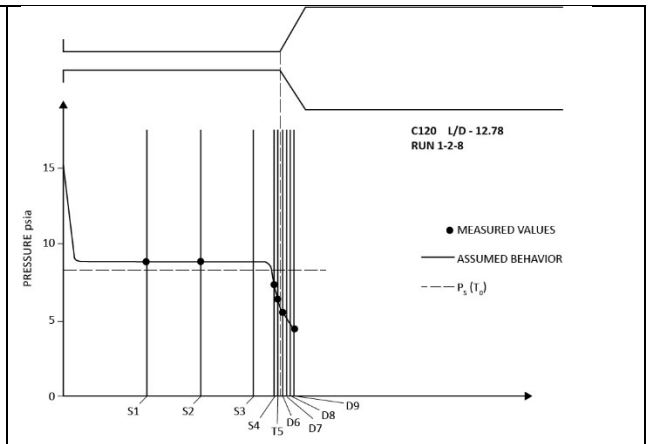

Figure 11.2.8b, Prisco Nozzle C120

Figure 11.2.8, Prisco (1975, Figure 4.3a) Measured Pressure Profiles

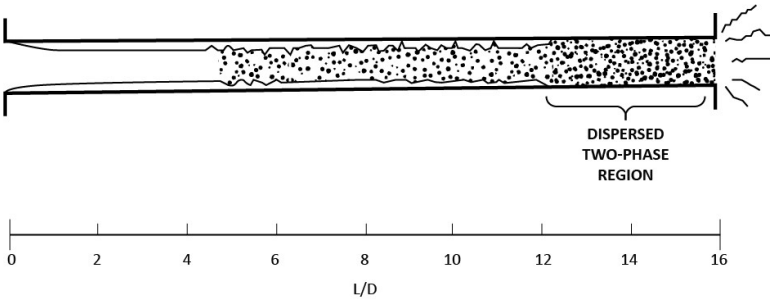

Figure 11.2.9, Prisco (1975) Flow Pattern

If the flow is a superheated jet flowing down the center of the constant-diameter portion of the nozzle, with choking essentially located at the exit plane, then the mass flow rate data can be evaluated using the Bernoulli equation for liquid flow with the downstream pressure equal to the *vena contracta* pressure and the flow area equal to the *vena contracta* cross-sectional area. The pressure measured at the pressure tap nearest to the inlet of the nozzle, P_{sx} in Figure 11.2.7, was used to approximate the *vena contracta* pressure and the flow area was estimated using the jet velocity ratio, from Equation

11.2.1. The results of these calculations are illustrated in Figure 11.2.10. The calculated mass flow rate agrees well with the measured flow rate. This result further substantiates the viewpoint that flow detachment occurs at the square-edged entrance plane and forms a superheated fluid core flowing down the center of the nozzles. The pressure in the liquid core is thus equal to the stagnation pressure minus acceleration losses and there is negligible wall friction. The saturated vapor annulus surrounding the superheated fluid core is, for all practical purposes, stagnant. Pressure measurements along the length of the constant-diameter portion of the nozzles and high speed videos from a transparent test section by Prisco substantiate this conclusion.

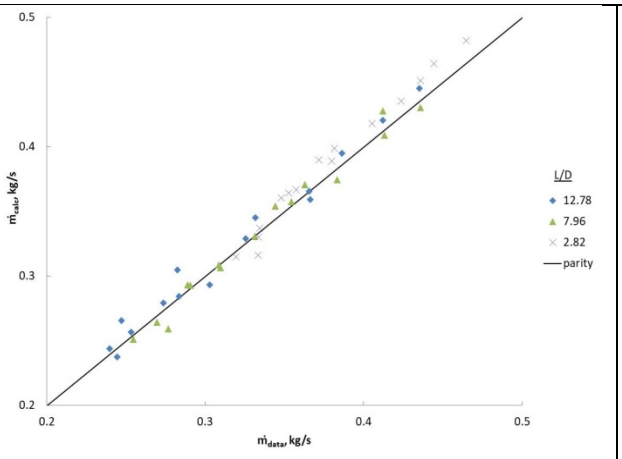

Figure 11.2.10a, Prisco Nozzle C7

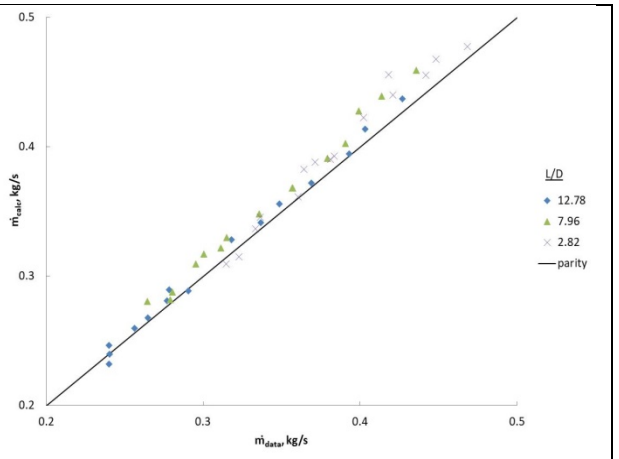

Figure 11.2.10b, Prisco Nozzle C120

Figure 11.2.10, Mass Flow Rate Calculated using *Vena Contracta* Conditions for Prisco (1975) Nozzles

The experimental protocol followed by Prisco involved adjusting operating conditions such that choking occurred at the nozzle exit plane. The residence times in the straight sections of the nozzles are 30 – 65% of the Downwer-Zapolski relaxation times. Given no pressure drop in the straight sections, short residence times compared to the relaxation times and flashing in the exit plane of the nozzle, it is concluded that mass flux calculations using Bernoulli flow are appropriate. *Given the measured mass flow rate, a mass flux can be calculated based on the vena contracta cross-sectional area.* This mass flux is of course higher than that reported by Prisco, which is based on the nozzle inside diameter. Given the inlet fluid is saturated with soluble nitrogen, Burnell's equation becomes Equation 11.2.15 with "P_s" equal to the equilibrium pressure of nitrogen above the R-11.

$$G = \sqrt{2\rho C P_s} \tag{11.2.15}$$

and

$$\Delta P_{Burnell} = C P_s \tag{11.2.16}$$

The "Burnell pressure drop" is defined as the pressure drop calculated using the Burnell equation required to match the experimental mass flux and is compared to the measured pressure drop in Figure 11.2.11. It is observed in these plots that pressure drop is matched better with the nozzle C7 data than with nozzle C120. One possible reason that the calculations match the data for nozzle C7 better than that for nozzle C120 is because of the location of the exit pressure taps. The exit pressure tap was located at the nozzle exit plane in nozzle C7 but it was slightly upstream (0.25 mm, 0.010 inch) of the exit plane in nozzle C120. Rapid depressurization, and likely flashing, occurred slightly upstream of the exit plane in the Nozzle C120 experiments.

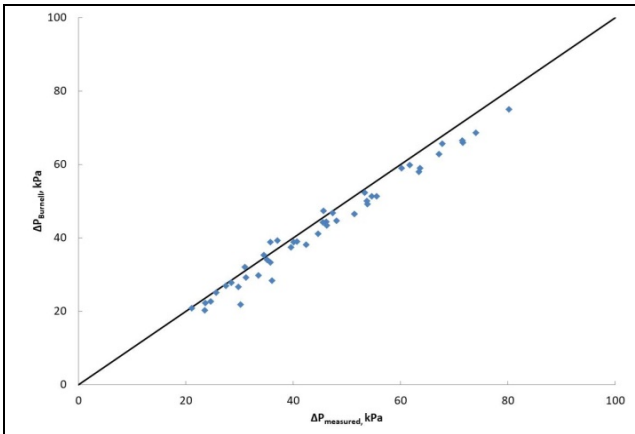

Figure 11.2.11a, Prisco Nozzle C7

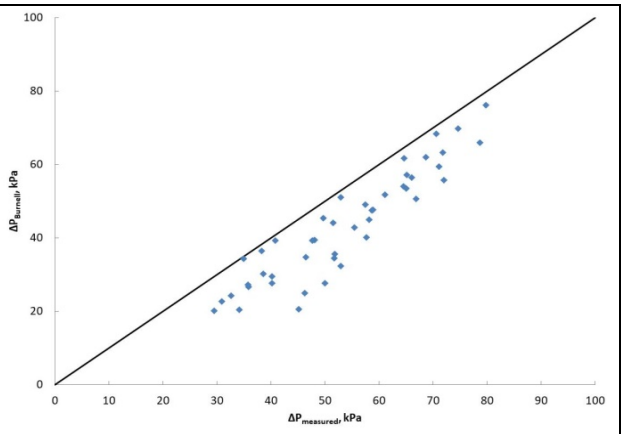

Figure 11.2.11b, Prisco Nozzle C120

Figure 11.2.11, "Burnell pressure drop" versus Measured Pressure Drop for Prisco (1975) Nozzles

The bubble nucleation method can be used to correlate the Burnell calculation results. The R-11 depressurization diagram with Prisco Nozzle C7 data for L/D = 2.82 is illustrated in Figure 11.2.12. The diagram was developed using scaling of the Gibb's number as previously discussed. Depressurization rates were selected to encompass the range of values indicated by Prisco's data. Figure 11.2.12a shows the entire diagram while Figure 11.2.12b shows the portion of the diagram where experimental data are located. One can see reasonable agreement between the data and nucleation theory calculation results. The curves for various depressurization rates practically coincide because of the small depressurization rates. *It is important to note that the agreement was achieved by properly accounting for the nitrogen partial pressure.* The calculated pressures were adjusted by adding the nitrogen partial pressure to the pressure drop calculated using the Alamgir and Lienhard correlation.

$$(P_s - P_{n,adjusted}) = \left[(P_s - P_{n,A-L}) + P_{Nitrogen}\right] \tag{11.2.17}$$

This result is equivalent to application of the bubble nucleation theory with a dissolved inert gas, wherein the pressure inside the bubble is equal to the vapor pressure of the fluid plus the partial pressure of inert gas.

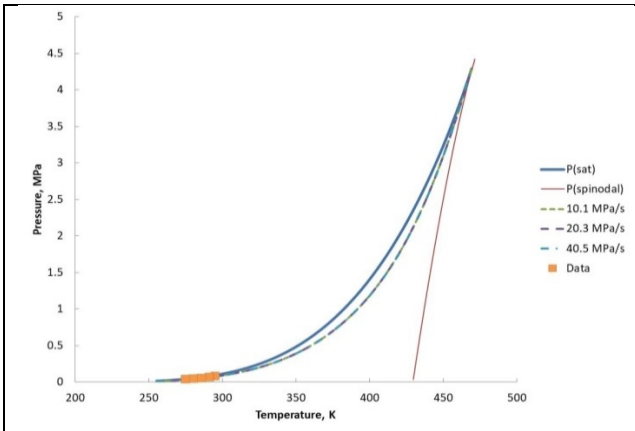

Figure 11.2.12a, R-11 Depressurization Diagram

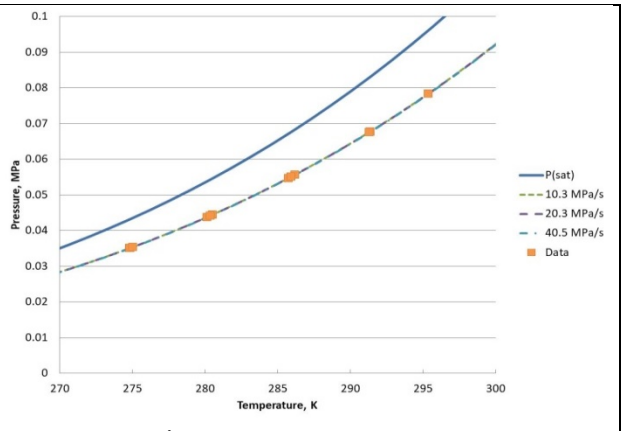

Figure 11.2.12b, R-11 Depressurization Diagram Expanded to show Data Region

Figure 11.2.12, R-11 Depressurization Diagram for Prisco (1975) Nozzle C7, L/D = 2.82

Application of the nucleation theory for R-11 is illustrated in Figures 11.2.13 and 11.2.14. In Figure 11.2.13 the calculated nozzle outlet pressure for Nozzle C7 shows good correlation with the measured data while the correlations show more deviation for Nozzle C120. *In Figure 11.2.14 the mass fluxes are based on the vena contracta cross-sectional area.* The bubble nucleation method shows reasonable agreement with the data for both nozzle geometries. Some dependence on nozzle length is observed. It is speculated that the nozzle length dependence is due to relaxation phenomena because the residence time in the nozzle straight section is equivalent to about 1 relaxation time for L/D = 2.82 and about 2.5 relaxation times for L/D = 12.78 according to the Downer-Zapolski correlation. (Increased relaxation time results in increased flashing pressure at constant temperature because the fluid has more time to "recover" from the pressure-undershoot and approach equilibrium.) Finally, the Burnell C factor calculated using the experimental data (axis labelled "Burnell C") is compared to the Burnell C factor calculated using the nucleation theory in Figure 11.2.15. The observations regarding exit pressure trends also apply to the Burnell C factor comparisons. It is important to note the inlet saturation pressure was used to calculate the Burnell C factors rather than the R-11 vapor pressure because of the nitrogen saturation of the R-11 in the feed vessel.

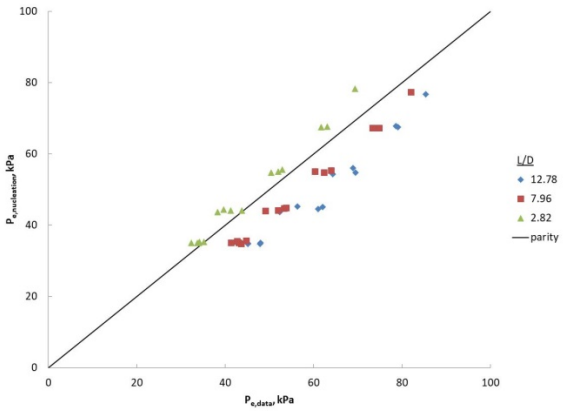

Figure 11.2.13a, Prisco Nozzle C7

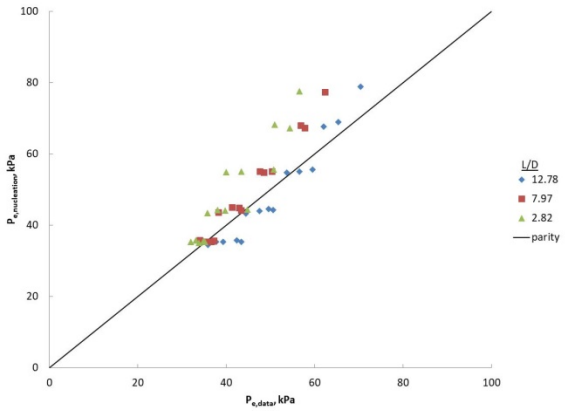

Figure 11.2.13b, Prisco Nozzle C120

Figure 11.2.13, Prisco (1975) Nozzle Outlet Pressure

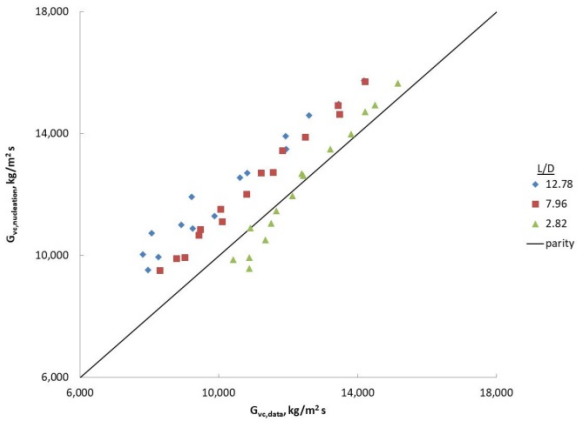

Figure 11.2.14a, Prisco Nozzle C7

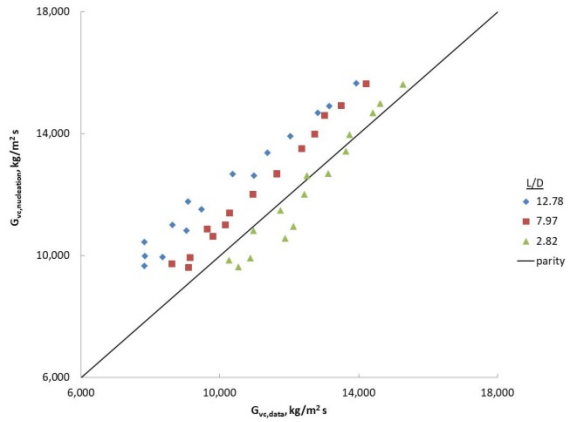

Figure 11.2.14b, Prisco Nozzle C120

Figure 11.2.14, Prisco (1975) Nozzle Mass Fluxes based on *Vena Contracta* Area

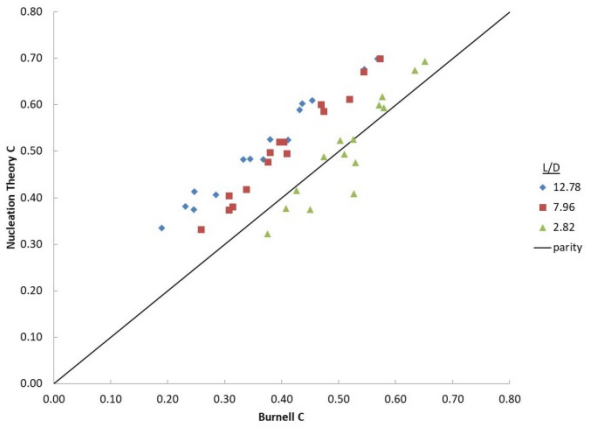

Figure 11.2.15a, Prisco Nozzle C7

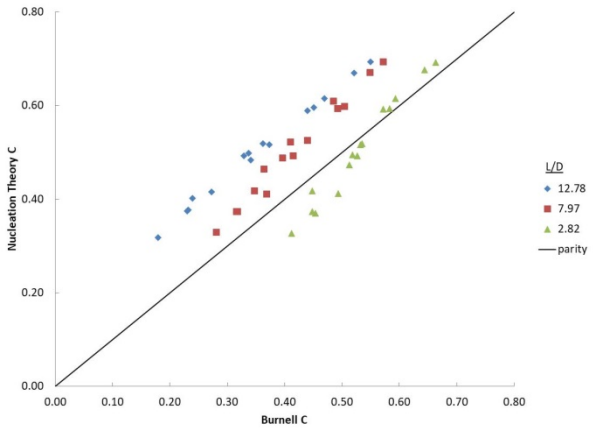

Figure 11.2.15b, Prisco Nozzle C120

Figure 11.2.15, Prisco (1975) Nozzle Burnell C Factor Values

12. Conclusions

Unification of bubble nucleation kinetics and thermodynamic stability analyses used to describe Rapid Phase Transitions (RPT), Boiling Liquid Expanding Vapor Explosions (BLEVE) and flow through nozzles provides a method to quantify non-equilibrium effects on calculated nozzle choking pressures and critical mass flow rates. The proposed method addresses known deficiencies of the Homogeneous Equilibrium Model for flow of saturated or slightly sub-cooled liquid through nozzles. Conclusions reached from the study of the Sozzi and Sutherland (1975) and Prisco (1975) data sets are:

1. Nozzle flow can approach equilibrium flow when:
    a. initial fluid temperature approaches the critical temperature because the amount of superheating due to rapid depressurization is constrained by the spinodal curve, e.g., less superheating is possible due to thermodynamic instability
    b. small rates of depressurization due to fluid acceleration occur, e.g., small available pressure driving force or appropriately rounded nozzle inlet geometries limit the maximum depressurization rate
    c. the local pressure is above the fluid vapor pressure at the location in the nozzle where the maximum depressurization rate occurs, e.g., at a given temperature, as the amount of subcooling increases due to increasing pressure, greater acceleration losses are required to decrease the local pressure to below the vapor pressure at the location of the maximum depressurization rate
    d. long residence time in the nozzle straight section downstream of the converging section allows enough time for relaxation
2. Otherwise, non-equilibrium flow should be considered for saturated or slightly subcooled liquid flow into a nozzle.
3. Proper accounting of fluid thermodynamic properties is essential. For example Prisco's experimental procedure included saturating the R-11 with nitrogen and thus all the test cases were necessarily run with saturated inlet conditions. Soluble inert gas complicates application of the bubble nucleation theory to determine the possible amount of fluid superheating because the partial pressure of inert gas increases the pressure inside of the nucleating bubbles above the fluid vapor pressure.

4. The “heterogeneity factors” for nozzle flow have mostly been developed for water–steam flow. It is plausible that methodical testing of fluids with a variety of physical properties may lead to heterogeneity factor correlations that depend on the fluid physical properties. Based on the limited number of tests analyzed herein, scaling of the Gibbs number relative to water and then application of the pressure-undershoot correlation from Alamgir and Lienhard (1981) provides reasonable estimates for the maximum expected amount of superheating due to rapid depressurization.
5. The inlet geometry of short nozzles plays a key role in the amount of superheating because the inlet geometry determines the maximum rate of depressurization for a given pressure driving force. Empirical correlations developed from data using nozzles with rounded inlets may not be applicable to nozzles with sharp-edged inlets because of geometry effects. In the case of rounded inlets (wherein no *vena contracta* is formed), the change in area with respect to distance (*dA/dz*) determines the maximum rate of depressurization. In the case of square-edged inlets, the fluid acceleration from the point of fluid detachment at the contraction plane to the *vena contracta* determines the maximum rate of depressurization.
6. Where a *vena contracta* is formed, it is important to note whether fluid reattachment downstream of the *vena contracta* occurs. In the case of short nozzles where fluid reattachment does not occur, the relevant flow area is the *vena contracta* cross-sectional area. Also without flow reattachment, there are no frictional losses along the nozzle wall. In the Prisco data analysis, the flow area can be represented by the cross-sectional area of the *vena contracta* because the flow did not reattach to the nozzle wall after the *vena contracta*. The data also indicates that application of a resistance coefficient for the sudden contraction is not appropriate in this situation.
7. Exit geometry can be the source of measurement error depending on the location of the exit pressure tap relative to the nozzle exit. In the Prisco nozzle C120 experiments, the presence or absence of exit plane choking was determined using a pressure tap 0.25 mm (0.010 inch) upstream of the exit plane while in the nozzle C7 experiments, the exit pressure tap was located at the exit plane. Given the rapid pressure drop upon flashing initiation at the nozzle exit, the *measured* “exit” pressures were 7 – 14 kPa (1 – 2 psi) lower in the C120 experiments than in the C7 experiments. This is likely due to the rapid pressure drop associated with flashing at the exit plane and the location of the pressure taps.
8. Models such as the Homogeneous Relaxation Model (HRM) should consider the amount of superheating due to rapid depressurization in the specification of the initial conditions for integration.

13. Summary

A bubble nucleation method to estimate the flow rate of saturated and slightly subcooled liquids through nozzles is proposed. The premises of the method are:

1. The available pressure driving force causes rapid depressurization of the fluid at the nozzle inlet due to the reduction in area available for flow determined by the nozzle geometry. The method is applied to both converging and square-edged inlet geometries by following the flow streamlines.
2. The amount of *potential* pressure-undershoot is determined using a pressure-undershoot correlation at the point in the nozzle where the maximum rate of depressurization occurs. The pressure-undershoot correlation is fluid composition dependent, as reflected by variation of the Gibbs number with composition.
3. The *realized* pressure-undershoot is determined by adjusting the *potential* pressure-undershoot with an approach to equilibrium “efficiency” based on the amount of superheating at the

location in the nozzle where the maximum depressurization rate occurs. The nozzle throat pressure is determined by the realized pressure-undershoot value.
4. Rapid vaporization occurs essentially at the nozzle throat after a bubble nucleation time delay resulting in choking at the nozzle throat.

One "skilled in the art" might immediately question various aspects of the proposed method, for example:

1. The pressure-undershoot correlation was developed for water and applied to other fluids using the Gibbs number.
2. The fluid inlet cannot be "too sub-cooled" because flashing will not occur in the nozzle (resulting in Bernoulli flow).
3. The nozzle cannot be "too short" because flashing will occur downstream of the nozzle due to the bubble nucleation time delay.
4. The nozzle cannot be "too long" because flashing may occur upstream of the nozzle throat due to the bubble nucleation time delay and because of fluid "relaxation" phenomena taking place.

The above list is purposely qualitative because it identifies areas for further research.

14. Recommendations for Further Work

Recommendations for further work are:

1. The Alamgir and Lienhard (1981) pressure-undershoot correlation was developed from rapid depressurization experimental data, for example see Alamgir, *et al.* (1980). The rapid depressurization experiments typically involved filling a closed tube with water, heating and pressurizing to the desired initial conditions, "bursting" open the outlet end of the tube and then measuring the depressurization rate and pressure-undershoot. Similar experiments with imposed backpressures are recommended to quantify the back pressure effect on depressurization rate and amount of pressure-undershoot. These experiments are recommended with a variety of other chemicals (including mixtures) to verify using the Gibbs number to scale the pressure-undershoot correlation.
2. Critical flow experiments with nozzles having various inlet geometries, e.g., varying the radius of curvature and beta ratio, are recommended to validate the interpretation of geometric effects changing the fluid streamlines and use of the maximum depressurization rate in the pressure-undershoot correlation. These experiments should also include a variety of other chemicals (including mixtures) to validate application to nozzle flow calculations of the pressure-undershoot correlation and the approach to equilibrium correlation. The nozzle lengths should also be varied to determine the location of flashing inception and the role of the boiling nucleation time delay.

15. Nomenclature

a_1, a_2 = constants to describe the vena contracta shape (Equations 11.2.2 and 11.2.3)
A = flow area
A_d = flow area downstream of the contraction plane
A_{min} = minimum nozzle flow area (nozzle throat or *vena contracta* area)
A_u = flow area upstream of the contraction plane
b_1 = constant to describe the vena contracta shape (Equations 11.2.2 and 11.2.3)
C = Burnell (1947) factor (Equation 4.1.1)
C_D = discharge coefficient
d = inside diameter
d_c = diameter in the nozzle converging portion
d_{vc} = diameter of the *vena contracta*
d_0 = small diameter
d_1 = upstream diameter
d_2 = downstream diameter
D = large diameter
f_D = Darcy (Moody) friction factor
g = acceleration of gravity
g_c = Newton's law conversion factor
G = mass flux
G_c = critical mass flux
Gb = Gibb's number (=W_{CR}/kT)
Gb_w = Gibbs number for water
h = vertical displacement
h_0 = (D-d)/2
h_{vc} = (d – d_{vc})/2
H_2 = head loss based on the smaller downstream diameter
J = nucleation rate
k = Boltzmann's constant
K_2 = head loss coefficient based on the smaller downstream diameter
l = length of nozzle constant-diameter portion
l_1 = distance from pipe contraction plane to upstream fluid separation point
l_2 = distance from pipe contraction plane to *vena contracta*
L = length of Sozzi and Sutherland nozzle converging section
$\dot{m}$ = mass flow rate
N = Fauske (1971) non-equilibrium factor (Equation 4.2.1)
P = pressure
P_0 = nozzle inlet pressure
P_a = normal atmospheric pressure
$P_{a,max}$ = pressure at the point of maximum depressurization rate
P_b = pressure inside a bubble
P_{Fi} = flashing inception pressure
P_n = bubble nucleation pressure
P_o = flashing onset pressure
P_s = fluid saturation pressure
P_s = fluid saturation pressure at location x in the nozzle
P_t = nozzle throat pressure (e.g., exit of the straight section)

P_u = fluid undershoot pressure
P_v = fluid vapor pressure
P_{vc} = nozzle pressure at the *vena contracta*
t = time
T = temperature
T_b = normal boiling point
T_c = thermodynamic critical temperature
T_i = inlet (initial) temperature
T_r = reduced temperature (T/T_c)
u = velocity
u_{vc} = jet velocity in the *vena contracta*
u_1 = upstream velocity
u_2 = downstream velocity
v = specific volume
v_f = fluid specific volume
v_g = gas specific volume
W_{CR} = net energy required to form a bubble [=$16\pi\sigma^3/3(\Delta P_c)^2$]
x = fluid quality
x_E = equilibrium fluid quality
x_0 = inlet quality
y = vertical distance above the bottom of the large pipe
y_d = vertical distance downstream of the contraction plane
y_u = vertical distance upstream of the contraction plane
z = axial distance
$z_{a,max}$ = location of maximum depressurization rate

β = diameter ratio
ϵ = void fraction
η = efficiency
$\eta_s = P_s/P_0$
$\eta_t = P_t/P_0$
θ = relaxation time
λ = jet velocity ratio
ρ = density
ρ_f = fluid density
ρ_g = gas density
ρ_t = fluid density at the nozzle throat
ρ_0 = fluid density at the nozzle inlet
σ = surface tension
Σ'_0 = depressurization rate
Σ'_0 = transient depressurization rate equal to zero for steady flows
τ = residence time
τ_d = residence time downstream of the contraction plane
τ_u = residence time upstream of the contraction plane
φ = bubble nucleation heterogeneity factor and Downer-Zapolski dimensionless pressure ratio
ψ = Downer-Zapolski dimensionless pressure ratio

Appendix A, Scaling Gibbs Number

Equation 10.3, repeated here for convenience, is used to estimate the Gibbs number for chemicals other than water.

$$Gb = Gb_w \left(\frac{\sigma}{\sigma_w}\right)^3 \frac{T_{c,w}}{T_c} \left[\frac{(P_{s,w} - P_a)}{(P_s - P_a)} \frac{\left(1 - \frac{\rho_{g,w}}{\rho_{f,w}}\right)}{\left(1 - \frac{\rho_g}{\rho_f}\right)} \right]^2 \Bigg|_{T_r = 0.9} \tag{10.3}$$

An estimation of the Gibbs number for R-11 is provided as an illustrative example. Variables used in Equation 10.3 are summarized in Table A1. All variables are evaluated at 0.9 times the critical temperature except the surface tension. The surface tension is evaluated at the R-11 normal boiling point.

Variable	water	R-11	ratio
T_c, K	647.31	471.38	1.3732
P_s at 0.9 T_c, Pa	9,760,222	2,147,442	
T_b, K	373.15	296.92	
P_a, Pa	101,325	101,325	
P_s-P_a, Pa	9,658,897	2,046,117	4.7206
ρ_g at 0.9 T_c, kg/m^3	53.83	122.04	
ρ_f at 0.9 T_c, kg/m^3	692.43	1088.38	
1-ρ_g/ρ_f	0.9223	0.8879	1.0387
σ at 297K, N/m	0.0721	0.0179	0.2476

Table A.1, Variable Summary

Substitution of relevant ratios into Equation 10.3 yields R-11 Gb=14.13.

$$Gb = 28.2 * 0.2476^3 * 1.3732 * (4.7206 * 1.0387)^2 = 14.13$$

Use of the Gibbs number to develop the depressurization diagram is accomplished by substitution into Equation 7.4 with the heterogeneity factor given by Equation 7.6.

$$\frac{Gb}{\varphi} = \frac{16\pi\sigma^3}{3kT(\Delta P)^2} \tag{7.4}$$

$$\varphi = 0.1058 T_r^{28.46} [1 + 14(\Sigma')^{0.8}] \tag{7.6}$$

The constant factor is given by

$$c = \sqrt{\frac{0.10588(16\pi)}{3(14.13)}} = 0.354 \tag{A.1}$$

Upon scaling for R-11, the estimated pressure-undershoot is given by

$$P_s(T_i) - P_n = 0.354 \frac{\sigma^{3/2} T_r^{13.73} \left[1+14\left(\Sigma'\right)^{0.8}\right]^{1/2}}{\sqrt{kT_c}\left(1-\frac{v_f}{v_g}\right)} \quad \text{(A.2)}$$

Appendix B, Bubble Nucleation Method Calculation Procedure

An illustrative example using water as the flowing fluid and the Sozzi and Sutherland (1975) nozzle 2 as the geometry is provided in this appendix. Relevant equations are Equation 7.7 to estimate the pressure-undershoot, Equation 10.1 to calculate the Burnell C factor, Equation 11.1.3 to calculate the flow area at the point of maximum depressurization rate, Equations 11.1.10 and 11.1.12 to estimate the maximum depressurization rate, Equation 11.1.13 to estimate the conversion "efficiency", and 11.1.14 to estimate the mass flux. The equations are repeated in the Appendix for convenience.

The first step is to determine the position in the nozzle where the maximum change in area versus position occurs, $\left(\frac{dA}{dz}\right)_{max}$ The maximum rate of pressure change, $\left(\frac{dP}{dt}\right)_{max}$, will occur at this position. Once this point is determined, the cross-sectional area, $A_{a,max}$, at that position should also be determined. Note for the Sozzi and Sutherland nozzle 2 geometry, from Equation 11.1.11, the maximum depressurization rate occurs at z = 37.656 mm (1.4711 inches). Note,the reader will need to determine the correct location of the maximum depressurization rate for specific nozzle geometries.

The second step is to determine an initial estimate of the mass flux. A convenient estimate is obtained using the Bernoulli equation (Equation 4.1.2) with the nozzle exit pressure equal to the fluid saturation pressure.

$$G_{guess} = \sqrt{\frac{2\rho_0[P_0 - P_s]}{1 + f_D\frac{l}{d}}} \tag{4.1.2}$$

$$\dot{m} = G_{guess} \cdot A_{min}$$

The proper area to use in the mass flow rate calculation is geometry dependent. In nozzles where flow separation (or detachment) does not occur, the throat area should be used. Where flow separation occurs the *vena contracta* area should be used if the vena contracta does not reattach and the throat area should be used if the *vena contracta* does reattach. Given an initial estimated flow rate the procedure is iterative, with the steps outlined below. The calculation sequence is as follows:

1. Calculate the pressure at the point of maximum acceleration ($P_{a,max}$) by subtracting the acceleration loss from the nozzle inlet pressure
$$P_{a,max} = P_0 - \frac{\rho u^2}{2} = P_0 - \frac{\dot{m}^2}{2\rho {A_{a,max}}^2}$$
2. Calculate the difference between the saturation pressure and pressure at the point of maximum acceleration.
$$P_{sat} - P_{a,max}$$
3. Calculate and the maximum depressurization rate (Σ') using Equation 11.1.10.

$$\left(\frac{dP}{dt}\right)_{max} = u\frac{dP}{dz} = \frac{\rho u^3}{A_{a,max}}\left(\frac{dA}{dz}\right)_{max} = -\frac{\dot{m}^3}{\rho^2 {A_{a,max}}^4}\frac{\pi^2 h_0}{2L}\left[D - 2h_0 sin\left(\frac{\pi z}{2L}\right)\right] cos\left(\frac{\pi z}{2L}\right) \tag{11.1.10}$$

$$\Sigma' = X_{units}\left(-\frac{dP}{dt}\right)_{max} \tag{11.1.12}$$

Note: Σ' must be in units of Matm/s. X_{units} is the appropriate unit conversion factor

4. Calculate *(P_{sat}-$P_{n,A-L}$)* using the Alamgir and Lienhard correlation (Equation 7.7)

$$P_s(T_i) - P_{n,A-L} = 0.252 \frac{\sigma^{3/2} T_r^{13.73} [1 + 14(\Sigma')^{0.8}]^{1/2}}{\sqrt{kT_c}\left(1 - \frac{v_f}{v_g}\right)} \tag{7.7}$$

5. Calculate the approach to equilibrium "efficiency" of converting $P_s(T_i) - P_{n,A-L}$ to the throat pressure using the correlation in Figure 11.1.10.

$$\eta = 0.736 \cdot \left(P_{sat} - P_{a,max}\right)[\text{MPa}] + 0.434$$

Note the maximum efficiency used is 1.0. Efficiency values greater than 1.0 are derived from the zero and 1.5 inch long nozzle data and not applicable for use in the current model because the flashing is believed to be occurring downstream of these short nozzles. This correlation is unit specific. The value of the difference between the saturation pressure and the pressure at maximum acceleration must be in MPa.

6. Calculate the "relaxed" pressure nucleation pressure $P_{n,relaxed}$ using Equation 11.1.13.

$$P_{n,relaxed} = P_{sat} - \eta(P_{sat} - P_{n,A-L}) \tag{11.1.13}$$

7. Using the nucleation pressure estimate from step 6, calculate an updated estimate of the mass flux using Equation 11.1.14.

$$G = \sqrt{\frac{2\rho_0\left(P_0 - P_{n,relaxed}\right)}{1 + f_D \frac{l}{d}}} \tag{11.1.14}$$

$$\dot{m}_{new} = G \cdot A_{min}$$

8. Repeat steps 1 – 7 until the estimated mass flux converges.

As a specific example, consider the geometry variables for the Sozzi and Sutherland nozzle 2 in Table B.1 and the fluid conditions provided in Table B.2. For the purposes of this example, isothermal flow of a constant density liquid was assumed. Physical properties used to calculate the nucleation pressure are evaluated at the saturated fluid temperature and pressure.

The mass flux initial estimate is

$$G\left(\frac{kg}{m^2 s}\right) = \sqrt{2 \cdot 753.28 \cdot \frac{(6{,}536{,}232 - 6{,}265{,}613)}{1.108}} = 19{,}182$$

With the Boltzmann constant k=1.38x10^{-23} J/K, the problem equations become

$$G(\tfrac{kg}{m^2 s}) = \sqrt{2 \cdot 753.28 \cdot (6{,}536{,}232 - P_n)/1.108} \tag{A2.1}$$

$$(P_s(T_i) - P_{n,A-L})(Pa) = 0.252 \frac{0.01937^{\frac{3}{2}} 0.8526^{13.73} \left[1 + 14(\Sigma')^{0.8}\right]^{\frac{1}{2}}}{0.9571\sqrt{(1.38x10^{-2})(647.096)}} = 841{,}310[1 + 14(\Sigma')^{0.8}]^{\frac{1}{2}} \tag{A2.2}$$

$$\Sigma'\left(\frac{Pa}{s}\right) = \frac{\dot{m}^3}{(753.28)^2(0.0001466)^4}\frac{\pi^2(0.01525)(0.01366)(0.2492)}{2(0.0445)} = 21{,}968{,}885 \cdot \dot{m}^3 \quad \text{(A2.3)}$$

The calculation results in Table B.3 show the convergence is adequate after about 20 iterations using direct substitution. This example took several iterations to converge because the initial estimate was far from the solution. The solution is readily found using modern methods to accelerate convergence. Finally, the Burnell C factor is estimated using Equation 10.1.

$$C = 1 - \frac{5.27}{6.26} = 0.1581$$

Converging section length (L), mm	44.5
Upstream diameter (D), mm	43.2
Downstream diameter (d), mm	12.7
Step height (h_0), mm	15.25
Maximum acceleration point (z), mm	37.3662
$\frac{\pi z}{2L}$	1.3190
$sin\left(\frac{\pi z}{2L}\right)$	0.9685
$cos\left(\frac{\pi z}{2L}\right)$	0.2492
$D - 2h_0 sin\left(\frac{\pi z}{2L}\right)$, mm	13.6619
Area at point of maximum acceleration (A_{max}), m^2	0.0001466
Nozzle area (A_n), m^2	0.0001267
Nozzle straight section length (l), mm	114.3
Friction factor (f_D)(Note 1)	0.012
$1+f_D l/d$	1.108

Table B.1, Geometric Variables

Note 1: The friction factor represents fully turbulent flow through a 12.7 mm inside diameter tube with a "smooth" surface, e.g., a surface roughness of 1.52 μm.

P_0, Pa	6,536,232
T_0, K	551.72
ρ_0, kg/m^3	753.28
σ, N/m	0.01937
P_s, Pa	6,265,613
T_s, K	551.72
T_c, K	647.096
T_r	0.8526
ρ_f, lb/ft3 (Note 1)	752.88
ρ_v, lb/ft3 (Note 1)	32.32
$1-v_f/v_g$	0.9571

Table B.2, Fluid Properties

Note 1: Fluid densities represent saturated fluid conditions at the stagnation enthalpy.

Iteration	**1**	**2**	**3**	**4**	**…**	**20**
Estimated G (kg/m^2 s)	19,182	28,613	32,866	35,359		41,389
$\dot{m}$ (kg/s) (=G*A_{nozzle})	2.430	3.625	4.163	4.479		5.243
$v_{a,max}$ (m/s)	22.01	32.82	37.70	40.56		47.48
$\rho u^2/2$ (Pa)	$0.18x10^6$	$0.41x10^6$	$0.54x10^6$	$0.62x10^6$		$0.89x10^6$
$P_{a,max}$ (Pa) (=P_0- $\rho u^2/2$)	$6.35x10^6$	$6.13x10^6$	$6.00x10^6$	$5.92x10^6$		$5.69x10^6$
Σ' (Pa/s), Equation A2.3	$3.15x10^8$	$1.05x10^9$	$1.59x10^9$	$1.97x10^9$		$3.17x10^9$
Σ' (Matm/s)	0.0031	0.0103	0.0156	0.0195		0.0312
$(P_s-P_n)_{Lienhard}$(Pa), Equation A2.2	$0.89x10^6$	$0.98x10^6$	$1.03x10^6$	$1.06x10^6$		$1.15x10^6$
P_s-$P_{a,max}$ (Pa)	-88,242	135,179	264,779	349,083		578,469
η (Figure 11.1.2.9)	0.3693	0.5337	0.6291	0.6912		0.8600
$(P_s-P_n)_{Relaxed}$(Pa), Equation 11.1.2.13	$0.33x10^6$	$0.53x10^6$	$0.65x10^6$	$0.74x10^6$		$0.99x10^6$
P_n, (Pa)	$5.93x10^6$	$5.74x10^6$	$5.62x10^6$	$5.53x10^6$		$5.27x10^6$
Calculated G, Equation A2.1	28,613	32,866	35,359	36,985		41,412

Table B.3, Illustrative Example

Bibliography

Abuaf, N., Jones, O.C., Jr., Wu, B.J.C., "Critical Flashing Flows in Nozzles with Subcooled Inlet Conditions", ASME J. Heat Transfer, 105(1983), 379-383, doi: https://doi.org/10.1115/1.3245589

Alamgir, Md., Kan, C.Y. and Lienhard, J.H., "An Experimental Study of the Rapid Depressurization of Hot Water", ASME J. Heat Transfer, 102(1980), 433-438, doi: https://doi.org/10.1115/1.3244318

Alamgir, Md. and Lienhard, J.H., "Correlation of Pressure Undershoot During Hot-Water Depressurization", ASME J. Heat Transfer, 103(1981), 52-55, doi: https://doi.org/10.1115/1.3244429

Angelo, E., Angelo, G., and Andrade, D.A., "A Mathematical Model for Metastable Condition Determination in Highly Flashing Liquid Flows Through Expansion Devices", Nucl. Eng. Design, 242(2012), 257-266, doi: https://doi.org/10.1016/j.nucengdes.2011.09.039

Avedisian, C.T., "The Homogeneous Nucleation Limits of Liquids" J. Phys. Chem Ref. Data, 14(1985), 695-729, doi: https://doi.org/10.1063/1.555734

Barbone, R., "Explosive Boiling of a Depressurized Volatile Liquid", Master in Engineering Thesis, McGill University (1994), doi: https://escholarship.mcgill.ca/concern/theses/0v838257w

Bartosiewicz, Y., Seynhaeve, J-M., and Serre, G., "Delayed Equilibrium Model and Validation Experiments for Two-Phase Choked Flows Relevant to LOCA", NURETH14-228 (2011), doi: https://doi.org/10.3139/124.110239

Benedict, R.P., "Fundamentals of Pipe Flow", John Wiley and Sons, New York (1980)

Benjamin, M.W. and Miller, J.G., "The Flow of a Flashing Mixture of Water and Steam through Pipes, Trans ASME, 64(1942), 657-664

Bilicki, Z. and Kestin, J., "Physical Aspects of the Relaxation Model in Two-Phase Flow", Proc. Royal Soc. A, 428(1990), 379-397, doi: https://doi.org/10.1098/rspa.1990.0040

Blander M. and Katz, J. L., "Bubble Nucleation in Liquids", AIChE Journal, 21(1975), 833-848, doi: https://doi.org/10.1002/aic.690210502

Brennen, C.E., "Cavitation and Bubble Dynamics", Oxford University Press, New York (1995), https://authors.library.caltech.edu/25017/5/BUBBOOK.pdf

Bullen, P.R., Cheesman, D.J., and Hussain, L.A. "A Study of Turbulent Flow in Pipe Contractions", Proc. Instn. Mech. Eng., Part E: J. Proc. Mech. Eng., 210(1996), 171-180, doi: https://doi.org/10.1243/PIME_PROC_1996_210_312_02

Burnell, J.G., "Flow of Boiling Water through Nozzles, Orifices, and Pipes", Engineering, 164 (1947), 527-576

De Lorenzo, M., Lafon, Ph., Seynhaeve, J. –M., and Bartosiewicz, Y., "Benchmark of Delayed Equilibrium Model (DEM) and Classic Two-phase Critical Flow Models Against Experimental Data", Int. J. Multiphase Flow, 92(2017), 112-130, doi: https://doi.org/10.1016/j.ijmultiphaseflow.2017.03.004

Downer-Zapolski, P., Bilicki, Z., Bolle, L. and Franco, J., "The Non-Equilibrium Relaxation Model for One-Dimensional Flashing Liquid Flow", Int. J. Multiphase Flow, 22(1996), 473-483, doi: https://doi.org/10.1016/0301-9322(95)00078-X

Fauske, H. K., "Contribution to the Theory of Two-Phase, One-Component Critical Flow", ANL-6633, October 1962, DOI: 10.2172/4749073

Fauske, H.K., "Flashing Flows or: Some Practical Guidelines for Emergency Release", Plant/Oper. Prog., 4(1985), 132-134, doi: https://doi.org/10.1002/prsb.720040304

Ferrari, A., Fluid Dynamics of Acoustic and Hydrodynamic Cavitation in Hydraulic Power Systems, Proc. Royal Soc. A, 473(2017), 20160345, doi: https://doi.org/10.1098/rspa.2016.0345

Henry, R.E. and Fauske, H.K., "The Two Phase Critical Flow of One Component Mixtures in Nozzles, Orifices, and Short Tubes", ASME J. Heat Transfer, 95(1971), 179-187, doi: https://doi.org/10.1115/1.3449782

Hodkinson, B., "The Flow of Hot Water through a Nozzle", Engineering, London, 143(1937), 629-630

Hutcherson, M.N., “Contribution to the Theory of the Two-Phase Blowdown Phenomenon”, ANL-75-82, 1975, https://inldigitallibrary.inl.gov/Reports/ANL-75-82.pdf
Hsu, Y. Y. “Review of critical flow, propagation of pressure pulse, and sonic velocity”, NASA TN D-6814 (1972), https://ntrs.nasa.gov/api/citations/19720019314/downloads/19720019314.pdf
Jones, O.C., Jr, and Saha, P., “Non-Equilibrium Aspects of Water Reactor Safety, Thermal Hydraulics Aspects of Nuclear Reactor Safety, Volume 1, Light Water Reactors”, ASME, New York, (1977), 249-288
Jones, O.C., Jr., “Flashing Inception in Flowing Liquids”, ASME J. Heat Transfer, 102(1980), 439-444, doi: https://doi.org/10.1115/1.3244319
Jones, O.C., Jr. “Toward as Unified Approach for Thermal Nonequilibrium in Gas-Liquid Systems”, Nucl. Eng. Des., 69(1982), 57-73, doi: https://doi.org/10.1016/0029-5493(82)90281-3
Kim, Y.-S., “A proposed correlation for critical flow rate of water flow”, Nuclear Engineering and Technology, 47(2015a), 135-138, doi: https://doi.org/10.1016/j.net.2014.11.004
Kim, Y.-S., “Overview of Geometrical Effects on the Critical Flow Rate of Sib-Cooled and Saturated Water”, Annals Nucl. Energy, 76(2015b), 12-18, doi: https://doi.org/10.1016/j.anucene.2014.09.028
Lackmé, C., “Incompleteness of the Flashing of Supersaturated Liquid and Sonic Ejection of the Produced Phases”, Int. J. Multiphase Flow, 5(1979), 131-141, doi: https://doi.org/10.1016/0301-9322(79)90041-7
Leung, J.C. and Ciolek, W.H., “Flashing Flow Discharge of Initially Subcooled Liquid in Pipes”, J. Fluids Eng., 116(1994), 643-645, doi: https://doi.org/10.1115/1.2910325
Leung, J.C., “A Correlation for Subcooled, Saturated and Low-quality Critical Discharge in Nozzles and Short Tubes”, DIERS Users Group Meeting, Burr Ridge, IL, September 16, 2019
Levy, S. and Abdollahian, D., “Homogeneous Non-Equilibrium Critical Flow Model”, Int. J. Heat and Mass Transfer, (25)1982, 759-770, doi: https://doi.org/10.1016/0017-9310(82)90088-6
Lienhard, J.H., Shamsundar, N. and Biney, P.O., “Spinodal Lines and Equations of State: A Review”, Nucl. Eng.Des., 95(1986), 297-314, doi: https://doi.org/10.1016/0029-5493(86)90056-7
Marviken Full Scale Critical Flow Tests, Joint Reactor Safety Experiments in the Marviken Power Station Sweden, NUREG/CR-2671 (1982)
Melhem, G. and Hendrickson, G., “Quantify Non-Equilibrium Flow and Rapid Phase Transitions”, ioMosaic Corporation Technical Paper, 2020
Mengmeng, X., “Thermodynamic and Gas Dynamic Aspects of a BLEVE”, PhD Thesis, Delft University of Technology, 2007, doi: http://resolver.tudelft.nl/uuid:a3514a6a-49d8-41b3-ada5-7a7dccb376ea
Miyatake, O., Tanaka, I. and Lior, N., “A Simple Universal Equation for Bubble Growth in Pure Liquids and Binary Solutions with a Non-Volatile Solute”, Int. J. Heat and Mass Transfer, (40)1997, 1577-1584, doi: https://doi.org/10.1016/S0017-9310(96)00224-4
Moody, F.J., “Maximum Discharge Rate of Liquid-Vapor Mixtures from Vessels”, presented in “Non-Equilibrium Two-Phase Flows”, ASME Heat Transfer Division Meeting, November 30 – December 5, 1975
Nilpueng, K. and Wongwises, S., “Experimental Investigation of Two-Phase Flow Characteristics of HFC-134a through Short Tube Orifices”, Int. J. Refrigeration, 32(2009), 854-864, doi: https://doi.org/10.1016/j.ijrefrig.2008.12.003
Powell, A.W., “Flow of Subcooled Water through Nozzles”, Westinghouse Electric Corporation, WAPD-PT-(V)-90, April 1961
Prisco, M.R., “The Nonequilibrium, Two-Phase Critical Discharge of Nearly Saturated and Subcooled CCl_3F through Short Tubes”, Argonne National Laboratory, ANL-75-9 (1975), https://www.osti.gov/servlets/purl/4202987
Rennels, D.C. and Hudson, H.M., “Pipe Flow, A Practical Comprehensive Guide”, John Wiley and Sons, New Jersey (2012), DOI: https://doi.org/10.1002/9781118275276

Reocreux, M., “Contribution a l’etude des debits critiques en ecoulement diphasique eau-vapor”, PhD Thesis, Université Scientifique et Medicale de Grenoble, France (1974), https://babel.hathitrust.org/cgi/pt?id=mdp.39015041730121&view=1up&seq=5

Riznic, J., Ishii, M. and Afgan, N., “A Void Distribution Model-Flashing Flow”, International seminar on transient phenomena in multiphase flow, Belgrade (Yugoslavia), CONF-8705150—1, DE87011430, 25-29 May 1987

Saha, P., “Review of Two Phase Steam-Water Critical Flow Models with Emphasis on Thermal Nonequilibrium, NUREG/CR 0417 & BNL-NUREG-50907 (1978)

Sallet, D.W. and Somers, G.W., “Flow Capacity and Response of Safety Relief Valves to Saturated Water Flow”, Plant / Operations Progress, 4(1985), 207-216, doi: https://doi.org/10.1002/prsb.720040405

Shin, T.S. and Jones, O.C., “Nucleation and Flashing in Nozzles – 1. A Distributed Nucleation Model”, Int. J. Multiphase Flow, 19(1993), 943-964, doi: https://doi.org/10.1016/0301-9322(93)90071-2

Silver, R. and Mitchell, J., “The discharge of saturated water through nozzles”, Transactions of North East Coast Institution of Engineers and Shipbuilders, 62(1945), 51-72

Simões-Moriera, J.R. and Shepard, J.E., “Evaporation Waves in Superheated Dodecane”, J. Fluid Mech., 382(1999), 63-86, doi: https://doi.org/10.1017/S0022112098003796

Sozzi, G.L. and Sutherland, W.A., “Critical Flow of Saturated and Subcooled Water at High Pressure”, General Electric, NEDO-13418, July 1975

Sudi, A., Aritomi, M., Murase, A. and Iwaki, K., “Relaxation Process of Thermal Non-Equilibrium in Boiling Two-Phase Flow (I)”, J. Nucl. Sci. Tech, 31(1994), 1171-1183, doi: https://doi.org/10.1080/18811248.1994.9735274

Vieira, M.M. and Simões-Moriera, J.R., “Low-Pressure Flashing Mechanisms in Iso-Octane Liquid Jets”, J. Fluid Mech., 572(2007), 121-144, doi: https://doi.org/10.1017/S0022112006003430

Weisman, J. and Tentner, A., “Models for estimation of critical flow in two-phase systems”, Prog. Nucl. Energy, 2(1978), 183-197, doi: https://doi.org/10.1016/0149-1970(78)90007-0

Yoon, H.J., Ishii, M., and Revankar, S.T., “Choking Flow Modeling with Mechanical and Thermal Non-Equilibrium”, Int. J. Heat and Mass Transfer, 49(2006), 171–186, doi: https://doi.org/10.1016/j.ijheatmasstransfer.2005.07.044